FISEVIER

Contents lists available at ScienceDirect

# Soil Dynamics and Earthquake Engineering

journal homepage: http://www.elsevier.com/locate/soildyn





# Coupled SPH-DEM simulations of liquefaction-induced flow failure

Usama El Shamy<sup>a,\*</sup>, Saman Farzi Sizkow<sup>b</sup>

- <sup>a</sup> Civil and Environmental Engineering Dept., Southern Methodist University, PO Box 750340, Dallas, TX, 75275, USA
- <sup>b</sup> Civil and Environmental Engineering Dept., Southern Methodist University, PO Box 750340, Dallas, TX, 75275, USA

#### ARTICLE INFO

# Keywords: Smoothed particle hydrodynamics Discrete element method Flow liquefaction Water film Shear localization Granular materials

#### ABSTRACT

A fully Lagrangian particle-based method for coupled fluid-particle interaction is utilized to evaluate flow liquefaction of saturated granular soils overlain by an impermeable crust. The solid particles are modelled as spherical particles using the discrete element method (DEM). The smoothed particle hydrodynamics (SPH) is employed to model the interstitial fluid using an averaged form of Navier-Stokes equations that accounts for the presence of the solid phase. The coupling between SPH and DEM is achieved through local averaging techniques and well-established semi-empirical formulas for fluid-particle interaction. The responses of loose and dense level granular deposits overlain by an impermeable crust to a seismic excitation are first analyzed. The loose deposit exhibited significant pore pressure development and liquefaction while the dense deposit barely showed any considerable buildup of pore pressure and did not liquefy. The formation of a water film was visible at the interface between the top crust and the underlying liquefied soil. When the same deposits were tilted to form an infinite slope, the loose deposit exhibited flow lgiquefaction at the location immediately underneath the impermeable crust and large shear strains accumulated within a thin layer immediately below the crust. Flow liquefaction was marked by dilative behavior at the surface of the liquefied sand and large lateral spreading that continued post-shaking. Void redistribution was observed along the loose deposit in the form of dilation for a thin layer near sand surface and contraction for the deeper depth. The dense sloping deposit did not liquefy and flow liquefaction was not observed.

## 1. Introduction

Liquefaction-induced flow failure represents an important mechanism that could lead to massive ground deformations. The National Research Council (NRC) in 1985 [1], defined four specific mechanisms of flow liquefaction. One of those mechanisms is particularly related to shear localization that occurs near the top of a liquefiable sand layer overlain by a surface low permeability crust in a sloping ground. In this scenario, void redistribution may occur in what was originally uniformly distributed void space, leading to the formation of loose sand zone at the top and denser zone near the bottom of the sand layer. The hypothesis is that as the top sand dilates, it attracts pore-water from the denser bottom layer. If a water interlayer forms at the interface between the impermeable crust and the underlying sand, the crust layer would move downslope at a large magnitude.

Strength loss due to void redistribution in a liquefiable layer overlain by an impermeable thin crust has been discussed in the literature by several researchers [e.g., [2–5]] and is shown schematically in Fig. 1.

Point (A) is near the surface of the liquefiable layer, while point (B) is near its base (Fig. 1a). Initially, the deposit is homogenous and the void ratio is the same along its depth (Fig. 1b). As shaking progresses, the lower part of the soil deposit (at B) densifies (Fig. 1b), resulting in upward water flow towards the interface between the overlying impermeable crust and the soil. The top part at (A) loosens and increases in volume (dilates) in response to the net upward flow (Fig. 1b). The upward flow creates a hydraulic gradient that causes the top layer to liquefy. The location at point (A) reaches a peak strength followed by a residual strength, while the location at point (B) gets denser and shows a reduction in the normalized stress ratio (Fig. 1c). The stress path shows that the vertical effective stress decreases at both locations in response to buildup in pore pressure (Fig. 1d). The soil at location (A) reaches the residual shear failure envelope and then it starts to flow (starting from point i) while the soil at (B) gains strength due to densification. The soil at (A) undergoes large downslope displacement that continues post-shaking. As the soil near location (A) continues to dilate, it attracts more water to the surface. The formation of a water interlayer at the

E-mail addresses: uelshamy@lyle.smu.edu (U. El Shamy), sfarzisizkow@smu.edu (S.F. Sizkow).

<sup>\*</sup> Corresponding author.

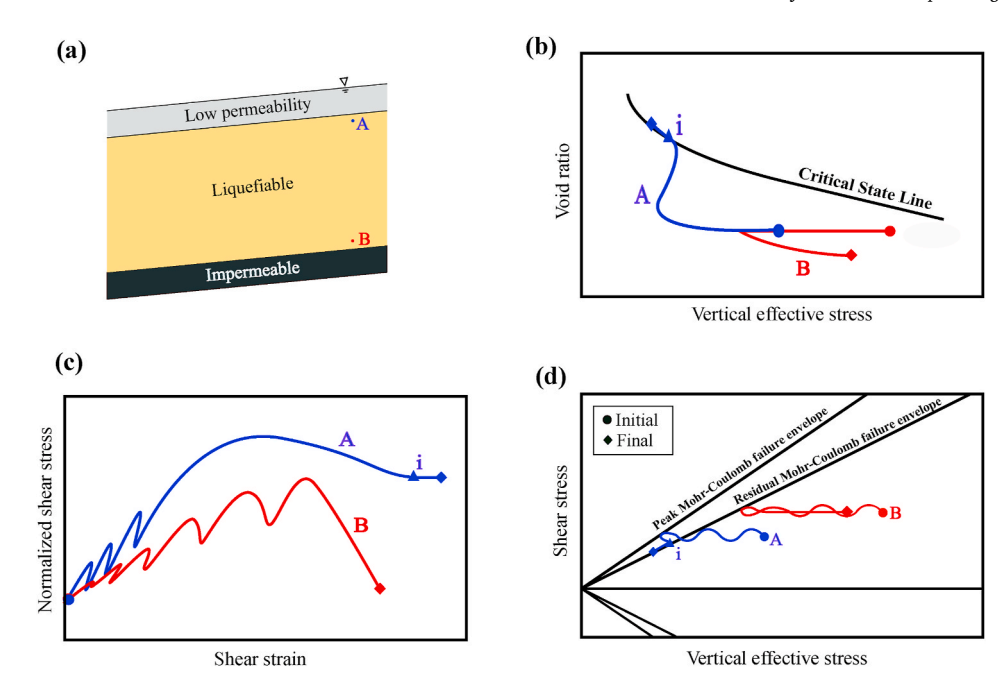


Fig. 1. Schematic responses of a liquefiable soil layer overlain by a low permeability crust (modified after [2]).

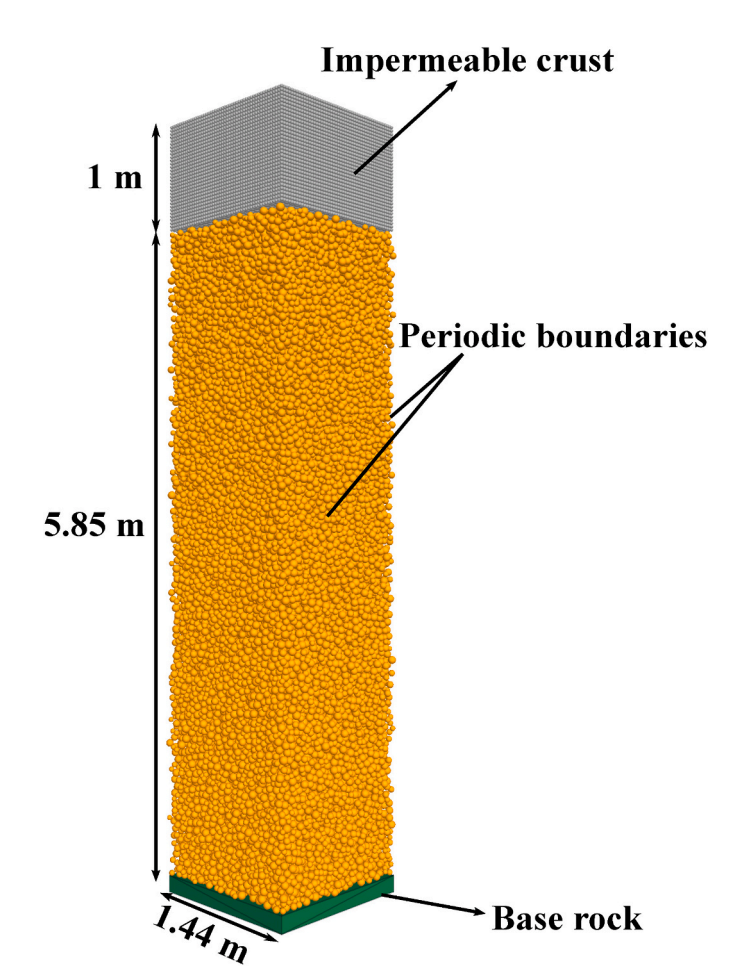


Fig. 2. 3D view of the saturated deposit in conducted simulations.

interface causes the crust layer to become unstable and moves downslope at excessive displacement magnitudes.

Various researchers have investigated the response of liquefiable

Table 1
Simulations details in model units.

Soil deposit	
Diameter (sand particles)	1.5 mm-2.5 mm
Diameter (crust)	1 mm
Normal stiffness	$5.0 \times 10^5 \text{ N/m}$
Shear stiffness	$5.0 \times 10^5 \text{ N/m}$
Normal critical damping ratio	0.1
Shear critical damping ratio	0.0
Friction coefficient	0.5
Rolling friction coefficient	0.2
Density (sand particles)	2650 kg/m <sup>3</sup>
Density (crust particles)	2054 kg/m <sup>3</sup>
Viscous Fluid	
Initial spacing	4 mm
Kernel radius	6 mm
Dynamic viscosity	0.6 Pa.s
Density	1000 kg/m <sup>3</sup>
Computation parameters	
g-level	30
Time step for DEM	$5 \times 10^{-7} \text{ s}$
Time step for SPH	$3.5\times10^{-6}~\text{s}$

slopes subjected to different types of loading through analytical studies [6–9], experimental works [4,6–8,10–21] and numerical modeling [3, 22–33]. A thorough discussion of these various techniques was presented by Boulanger et al. [2]. The main takeaways from the experimental studies are: (1) an upward flow of pore water forms in the liquefied sand that moves toward the overlying low permeability layer; (2) this upward flow leads to void redistribution and the creation of a thin dilating (loosening) zone immediately below the low permeability layer; (3) the void redistribution causes strain localization and large lateral deformations; and (4) the potential for void redistribution depends on the initial relative density, slope geometry, shaking duration, shaking amplitude, and shaking history [20].

Numerical modeling of the void redistribution process is a challenging task. Some of the factors contributing to its complexity are issues regarding localization length scale and ability of the constitutive models to effectively account for the loosening effects [2]. Ziotopoulou and Boulanger [32] presented a constitutive model called the PM4Sand based on the framework proposed by Dafalias and Manzari [25]. They made some modifications to the base model to improve its ability to

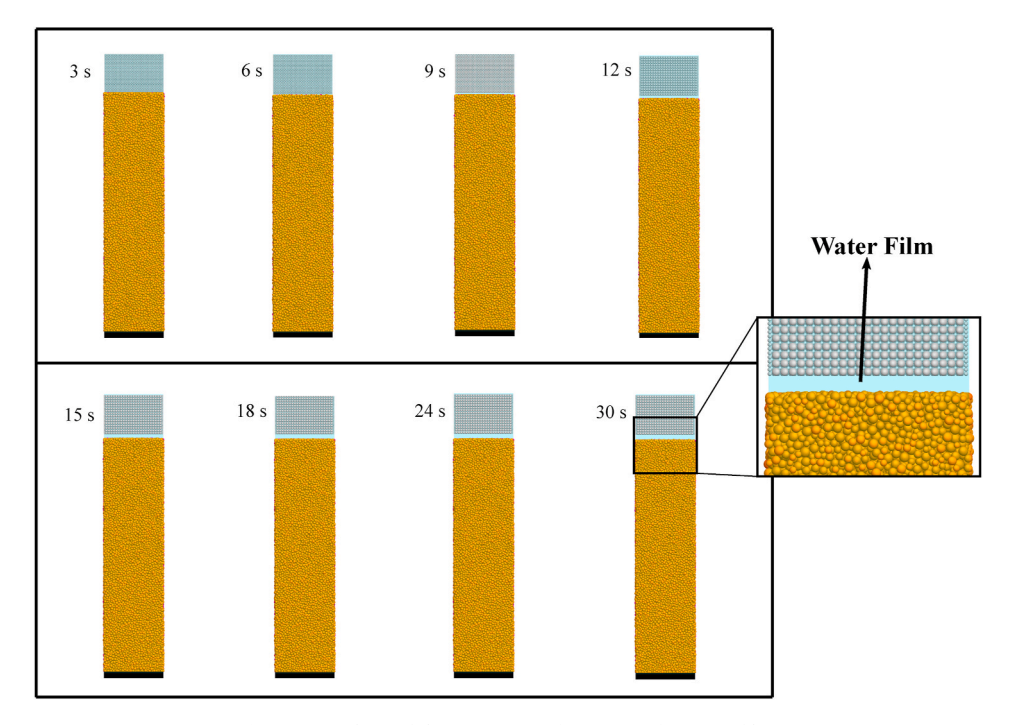


Fig. 3. Snapshots of the progressive formation of a water film.

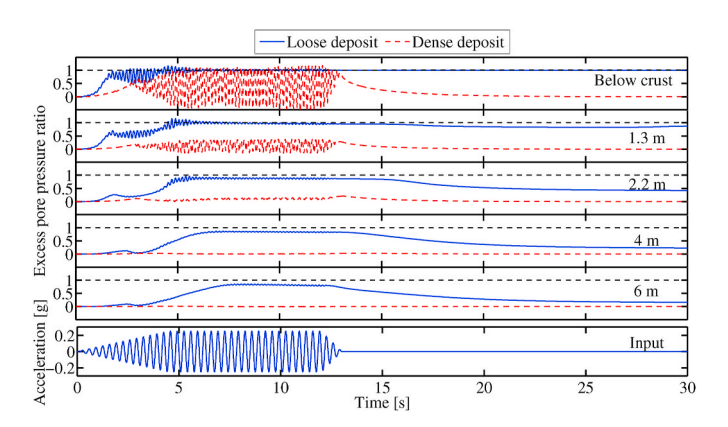
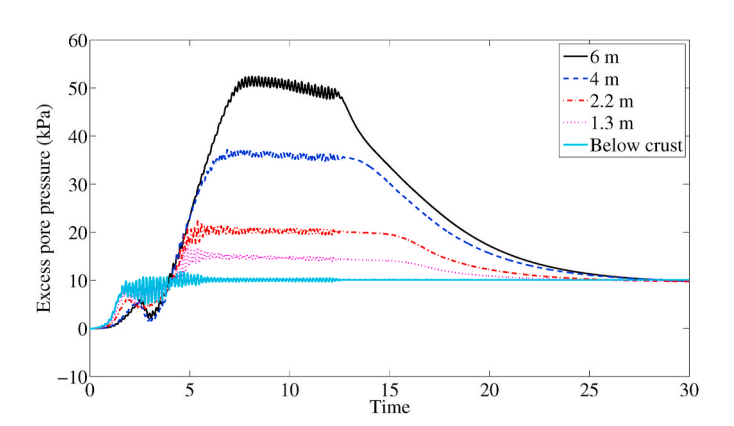
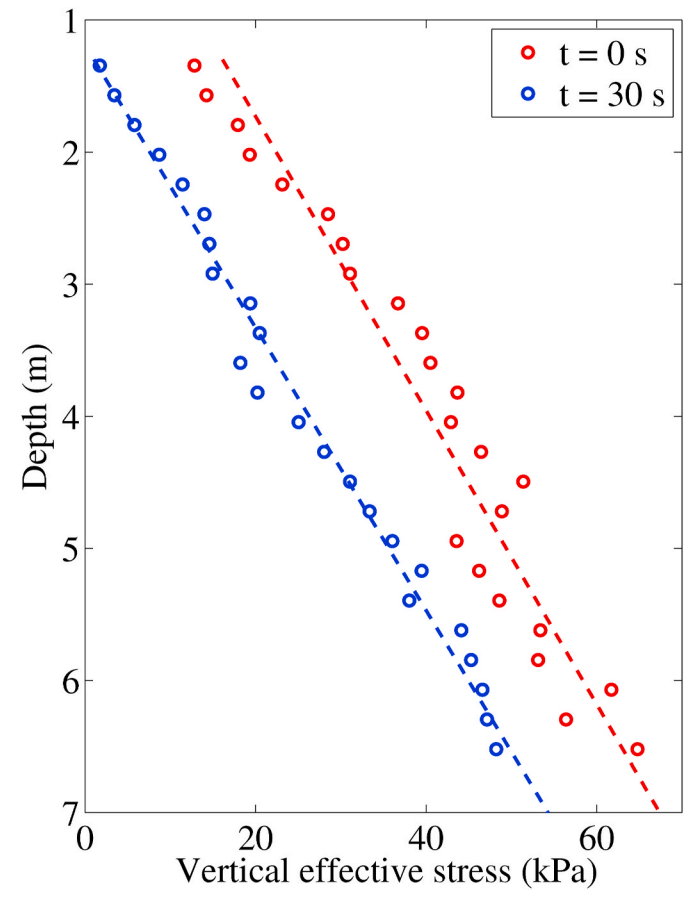


Fig. 4. Time histories of excess pore pressure ratio at selected depth locations.



**Fig. 5.** Time histories of excess pore water pressure at selected depth locations along the loose level deposit.



**Fig. 6.** Vertical effective stress profiles at the beginning and end of simulation for loose level deposit (the straight lines are least-squares best fit).

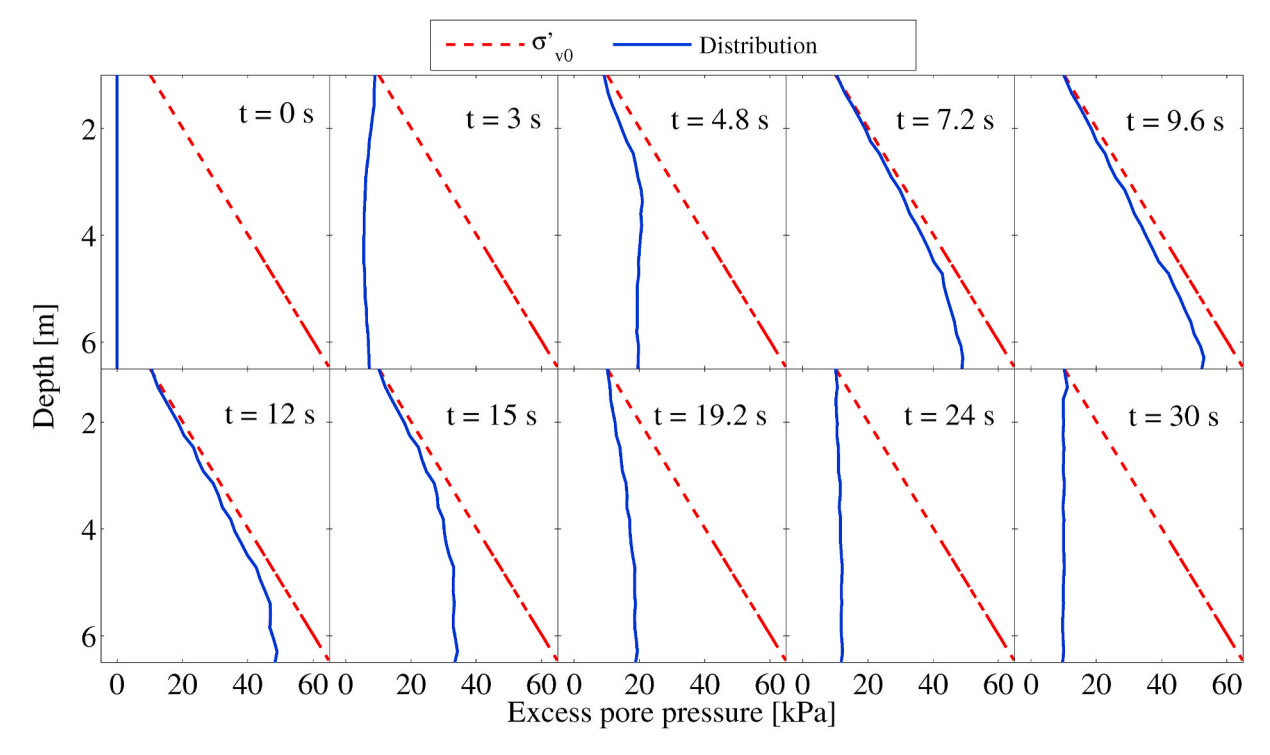


Fig. 7. Excess pore pressure profiles at selected time instants for the loose level deposit.

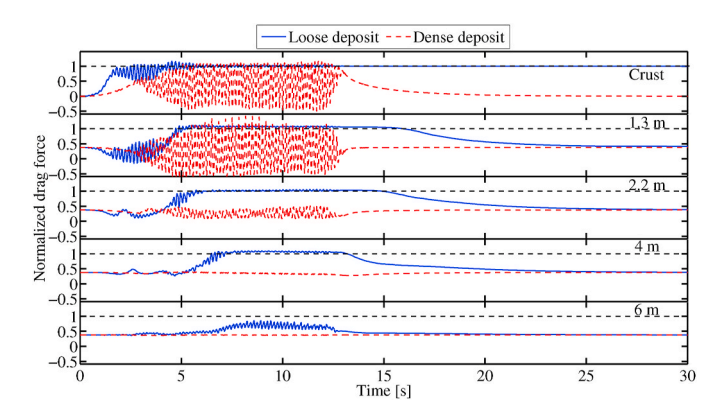


Fig. 8. Time histories of vertical fluid drag force normalized by the average particle weight at selected depths.

replicate commonly observed trends such as the effects of loading duration and overburden stress on the cyclic resistance ratio of sand. The main calibration parameters in this model are: (1) shear modulus coefficient; (2) apparent relative density; and (3) the contraction rate parameter. Several constitutive models have been presented to describe the behavior of saturated granular soils during cyclic loading [e.g., [34–41]]. Kamai and Boulanger [31] performed numerical simulations using PM4Sand constitutive model to study liquefaction-induced lateral spreading in two symmetric slopes overlain by clayey-silt crusts. They also conducted a sensitivity study regarding various parameters including cyclic strength and hydraulic conductivity. The simulations were successful at capturing some of the key trends observed in the experimental studies, notably a void redistribution pattern. Kamai [3] used PM4Sand model to investigate the response of a submerged slope with embedded silt layers. The results show void redistribution patterns and formation of a thin dilation zone immediately below the silt arc. The simulations were in reasonable agreement with the experimental results provided by Malvick et al. [4], but failed to reproduce the delayed, post-shaking deformations [3].

The discrete element method (DEM) can effectively model granular soils based on micromechanical considerations. This method [42] simulates these media as a packing of interacting discrete particles, and has shown the ability to reproduce the actual behavior of granular soils with few microscale parameters. Several techniques exist to account for fluid-particle interaction in the DEM formulation. One possibility is to describe the fluid flow at a macroscopic level by averaged Navier-Stokes equation based on mean mixture properties and employ well-established semi-empirical equations to calculate the fluid particle interaction forces [43–45]. This approach has been adopted by many researchers to model several problems in geomechanics [e.g., [46–50]].

A pore-scale (mesoscale) fluid model would be ideal to investigate the development of pore pressure due to actual changes in the shape and volume of the pore space caused by particle movements. Two of the most common techniques that have been applied to idealize the fluid at the pore-scale are the smoothed particle hydrodynamics (SPH) [e.g., [51, 52]] and the lattice Boltzmann method (LBM) [e.g., [53–55]]. The high accuracy of the pore scale models comes at the cost of being computationally expensive, to a degree that makes it impractical to perform numerical simulations with realistic particle sizes using typical desktop computers.

As an alternative to modeling the fluid at the pore-scale, SPH could be used to approximate the set of partial differential equations represented by an averaged form of Navier-Stokes equations [56,57] that accounts for the presence of the solid phase and the momentum transfer between the phases at a the macroscale. This approach was presented by Sun et al. [58] and was implemented in various science and engineering problems [e.g., [59–67]]. In this paper, the results of a novel application of SPH-DEM to model flow liquefaction is presented. SPH is used to model the fluid phase in which the domain is discretized into a group of individual particles carrying local properties of the fluid such as density and pressure [68-70]. DEM is employed to model the solid particles with proper momentum transfer between the two phases. A description of the model components were previously presented by the authors [71] and will be briefly described in the following section for completeness. The responses of level loose and dense level saturated granular deposits overlain by a thin impermeable crust to seismic excitation are first

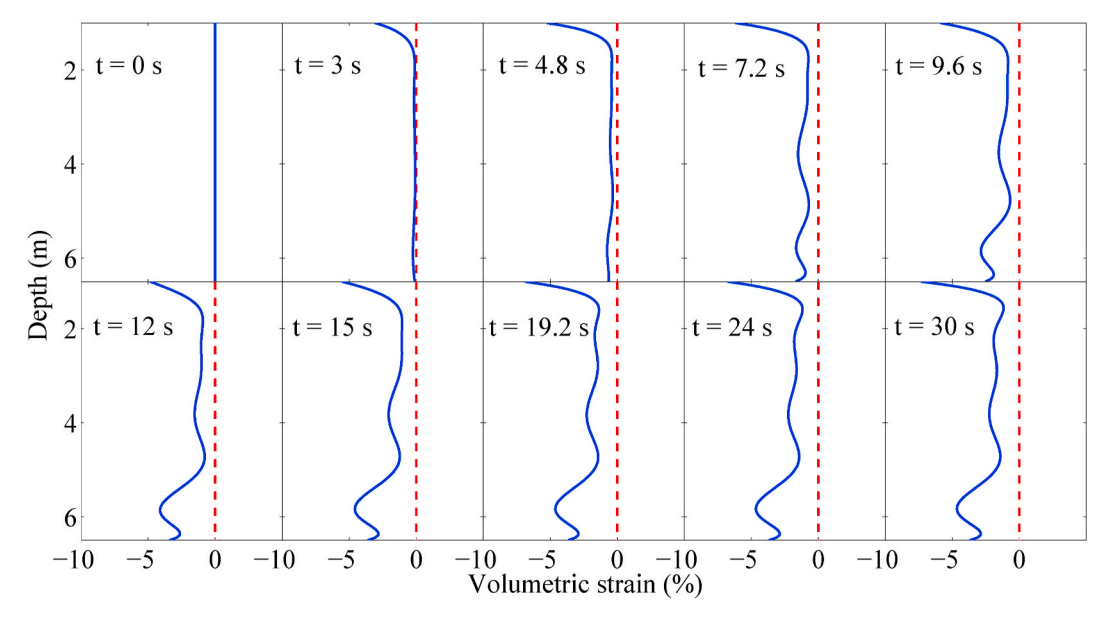


Fig. 9. Volumetric strain profiles at selected time instants for the loose level deposit.

analyzed. Then, the response of the same deposits when sloped is presented.

# 2. Coupled SPH-DEM model

The two-fluid model presented by Ref. [72] is used herein to describe the governing equations for fluid in the multiphase mixture [62]:

$$\frac{\partial(n\rho_f)}{\partial t} + \nabla \cdot (n\rho_f \mathbf{u}) = 0 \tag{1}$$

$$\frac{\partial (n\rho_f \mathbf{u})}{\partial t} + \nabla \cdot (n\rho_f \mathbf{u}\mathbf{u}) = -\nabla P + \nabla \cdot \mathbf{\tau} + n\rho_f \mathbf{g} - \mathbf{f}^{int}$$
(2)

in which  $\rho_f$  is the fluid density, n is the porosity, P is the fluid pressure,  $\tau$ is the viscous stress tensor,  $\mathbf{f}^{int}$  is the fluid particle interaction force,  $\mathbf{g}$  is the gravitational acceleration vector and  $\mathbf{u}$  is the fluid velocity.

In SPH, the continuum is lumped into discrete particles moving with the flow and each particle holds the information regarding the physical properties of the fluid. A kernel function (W) is then employed to interpolate different quantities at a given location. Herein, the Wendland kernel function is chosen as the smoothing function [73]. Applying SPH particle summation, Eqs. (1) and (2) can be rewritten as:

$$\frac{d(n_i\rho_i)}{dt} = \sum_i m_j \mathbf{u_{ij}} \cdot \nabla_i W(|\mathbf{r_{ij}}|, h)$$
(3)

$$\frac{d\mathbf{u_i}}{dt} = -\sum_{j} m_j \left[ \frac{P_i}{(n_i \rho_i)^2} + \frac{P_j}{(n_j \rho_j)^2} + R_{ij} \left( \frac{W(|\mathbf{r_{ij}}|, h)}{W(\Delta p, h)} \right)^4 \right] \nabla_i W(|\mathbf{r_{ij}}|, h) + \mathbf{\Pi}_{ij} + \frac{\mathbf{f^{int}}}{m_i}$$

with  $\mathbf{u}_{ii}$  being the relative velocity vector,  $P_i$  fluid pressure evaluated at the location of particle i,  $r_{ii}$  the tensile instability term to prevent particles from forming small clumps and  $\Pi_{ii}$  the non-artificial viscosity term [74,75]. Fluid pressure is computed using the weakly compressible equation of state, which provides a relationship between the fluid pressure and its density [76].

The solid phase was modeled as a collection of particles using DEM. To account for the effects of particle shape on the energy loss during rotational particle movements, the rolling resistance contact model was incorporated into DEM simulations by various researchers [78–81]. The

rolling resistance contact model employed in this study is based on the linear contact model that incorporates a torque acting on the contacting particles and resisting their rolling motions. The rolling resistance contact model behavior is similar to the linear contact model, except that relative rotation of contacting particles at the contact point produces an internal moment at the contact [78].

The total force exerted by the fluid on the solid particle a can be written as the sum of the drag force  $(F_a^D)$  and pressure gradient force  $(F_a^P)$ 

$$\mathbf{F}_{\mathbf{a}}^{\text{int}} = \mathbf{F}_{\mathbf{a}}^{\mathbf{D}} + \mathbf{F}_{\mathbf{a}}^{\mathbf{P}} \tag{5}$$

The drag force was estimated using the well-known equation recommended by Ergun [83]. This equation evaluates the drag force based on the local porosity and the relative velocity between fluid and solid

$$\mathbf{F}_{\mathbf{a}}^{\mathbf{D}} = \frac{\beta V_a}{1 - n_a} \left( \overline{\mathbf{u}}_{\mathbf{a}} - \mathbf{u}_{\mathbf{a}} \right) \tag{6}$$

where  $\beta$  is the interphase momentum exchange coefficient,  $\overline{\mathbf{u}}_{\mathbf{a}}$  is the average flow velocity around the solid particle a,  $V_a$  is the volume of the solid particle,  $\mathbf{u}_a$  is the velocity of the solid particle and  $n_a$  is the mean porosity. β follows two different regimes divided by the local porosity

$$\frac{d\mathbf{u}_{i}}{dt} = -\sum_{j} m_{j} \left[ \frac{P_{i}}{(n_{i}\rho_{i})^{2}} + \frac{P_{j}}{(n_{j}\rho_{j})^{2}} + R_{ij} \left( \frac{W(|\mathbf{r}_{ij}|, h)}{W(\Delta p, h)} \right)^{4} \right] \nabla_{i} W(|\mathbf{r}_{ij}|, h) + \mathbf{\Pi}_{ij} + \frac{\mathbf{f}^{int}}{m_{i}}$$

$$\beta = \begin{cases}
150 \frac{(1 - n_{a})^{2}}{n_{a}} \frac{\mu}{d_{a}^{2}} + 1.75(1 - n_{a}) \frac{\rho}{d_{a}} |\overline{\mathbf{u}}_{\mathbf{a}} - \mathbf{u}_{\mathbf{a}}| & n_{a} \leq 0.8 \\
0.75C_{d} \frac{n_{a}(1 - n_{a})}{d_{a}} \rho |\overline{\mathbf{u}}_{\mathbf{a}} - \mathbf{u}_{\mathbf{a}}| & n_{a} > 0.8
\end{cases}$$
(7)

in which  $\mu$  is the dynamic viscosity of the fluid,  $d_a$  is the solid particle diameter and  $C_d$  is the drag coefficient [83].

If the interaction between fluid and solid particles is the only source for the generation of pressure gradient, the total interaction force can be simplified as [82]:

$$\mathbf{F}_{\mathbf{a}}^{\text{int}} = \mathbf{F}_{\mathbf{a}}^{\mathbf{D}} + \mathbf{F}_{\mathbf{a}}^{\mathbf{P}} = \frac{\mathbf{F}_{\mathbf{a}}^{\mathbf{D}}}{n_{a}} - V_{a} \rho_{f} \mathbf{g}$$
(8)

Due to the momentum exchange with solid particles, a coupling force will also be applied to the fluid particle i which can be estimated by the weighted average of contributions from all surrounding DEM particles inside its influence domain:

(4)

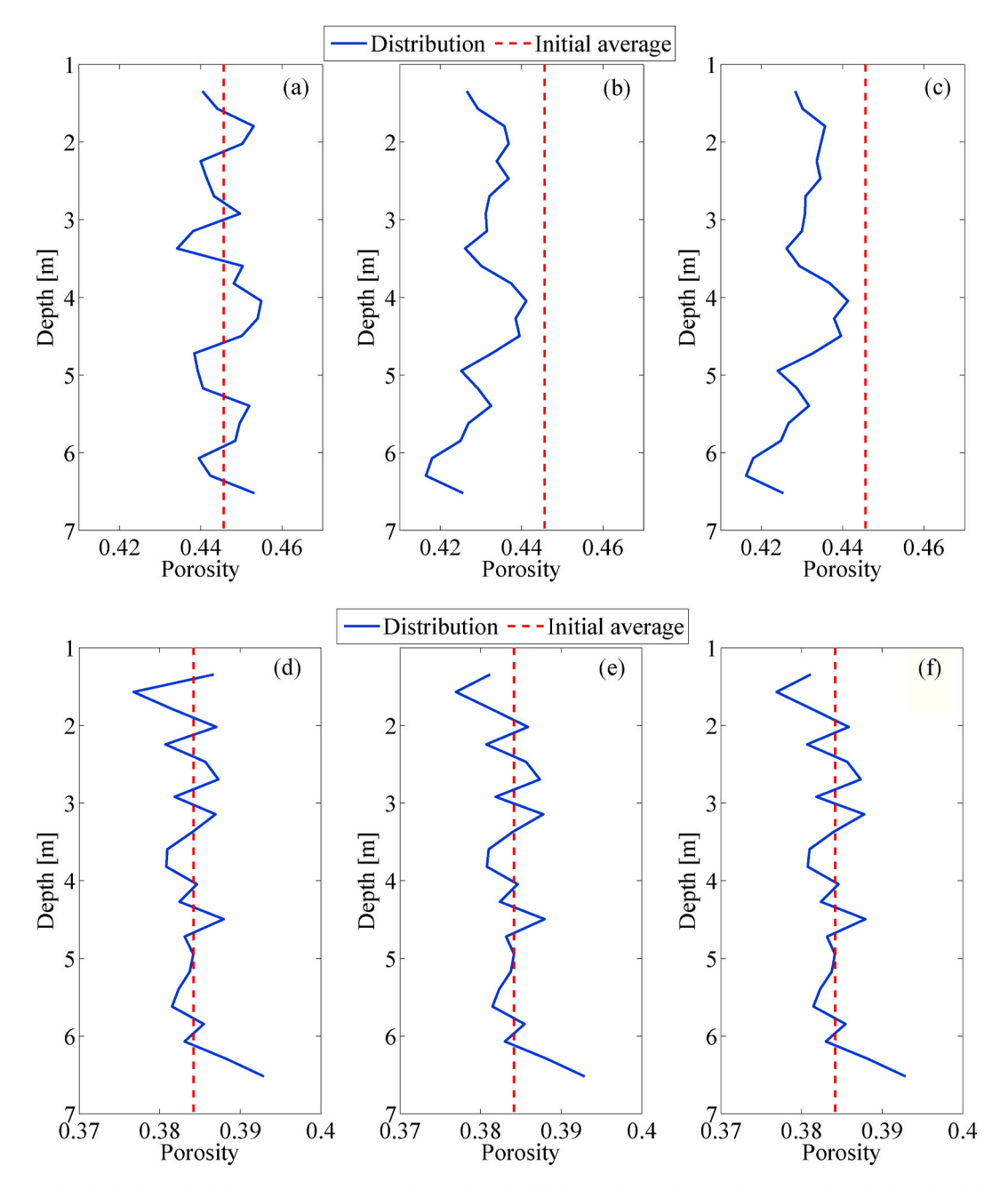


Fig. 10. Porosity profiles for the loose level deposit at a) start of simulation, b) end of shaking and c) end of simulation as well as the dense level deposit at d) start of simulation, e) end of shaking and f) end of simulation.

$$\mathbf{f_{i}^{int}} = -\frac{m_{i}}{\rho_{i}} \sum_{a} \frac{W(|\mathbf{r_{ai}}|, h)}{\sum_{j \stackrel{m_{j}}{\rho_{i}}} W(|\mathbf{r_{aj}}|, h)} \mathbf{F_{a}^{int}}$$
(9)

The PFC3D software [84] was used to perform the DEM aspects of the model. The software implements parallel computing for its DEM analysis. The SPH part of the coupled algorithm was carried out by a Cython code written by the authors and linked to the PFC3D environment. Use was made of the Open Multi-Processing (OpenMP) scheme to parallelize the SPH code and reduce the computational time. More details regarding the computational scheme as well as validation simulation of the proposed framework could be found in Ref. [71].

In view of the complexity of the goal of this study to model soil liquefaction of a saturated soil deposit, a building block approach [85] was adopted to validate the proposed coupled SPH-DEM model. That is, the components of the model were validated separately before combining all model components to idealize the system. This strategy

proved to be an effective approach to validate models in other engineering fields [86], and is usually dictated by the impracticality of conducting validation experiments on complex systems. The computational results of the model were, therefore, compared with the experimental and analytical data at multiple degrees of physics coupling. The ability of SPH to model Poiseuille flow was tested and validated [71]. The use of DEM to model dry granular deposited was demonstrated by the first author in an earlier publication [87]. The main coupling parameters between the fluid and particles in this model stem from porosity calculation, averaged solid particle velocities and the resulting drag force. Therefore, a simulation was performed to examine the ability of the model to correctly predict the drag force on a few settling particles in a fluid column [71]. Since this system has a diluted concentration of particles, it presents an extreme in computing porosity and associated drag forces. It also include the challenge of large solid particle velocities. Additionally, another extreme situation in which flow in a dense

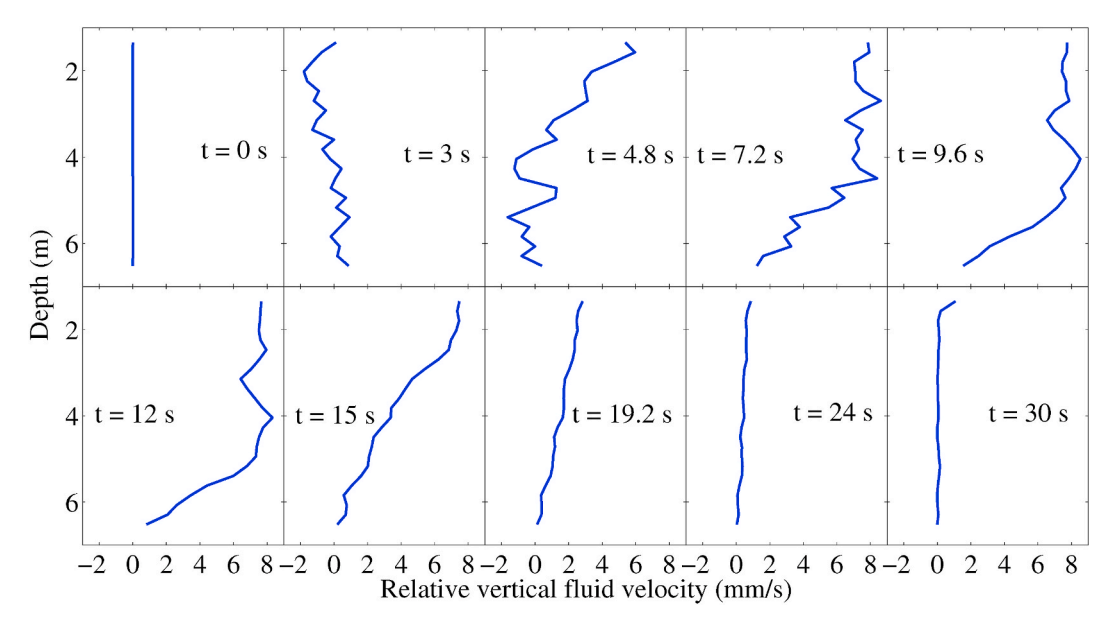


Fig. 11. Vertical fluid velocity profiles at selected time instants for the loose level deposit.

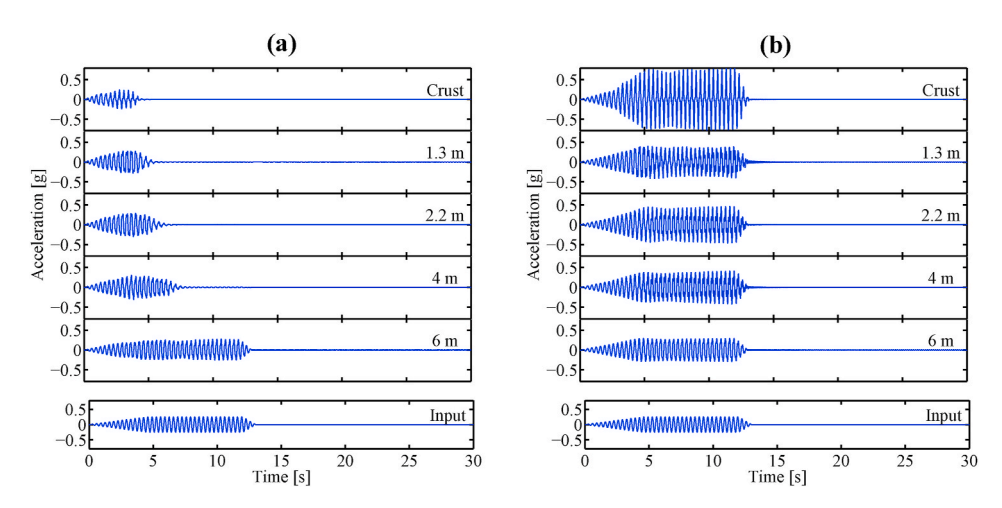


Fig. 12. Time histories of average horizontal acceleration at selected depths for: a) loose level deposit, and b) dense level deposit.

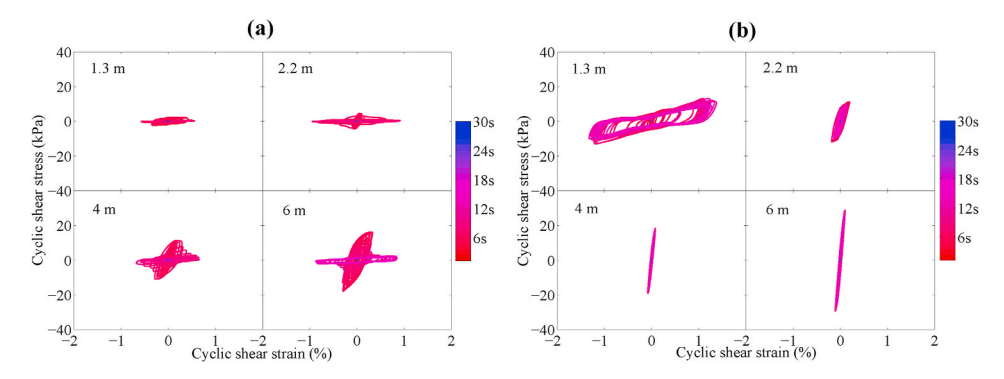


Fig. 13. Shear stress-strain loops at selected depths for: a) loose level deposit, and b) dense level deposit.

stagnant arrangement of a porous medium was considered to examine the ability of the fluid code to accurately predict fluid velocities in such a dense packing [88].

# 3. Simulations

The proposed SPH-DEM approach was utilized to study potential flow liquefaction and void redistribution of saturated granular deposits overlain by an impermeable crust. Two deposits were generated for this purpose, one was loose (and therefore susceptible to liquefaction) and

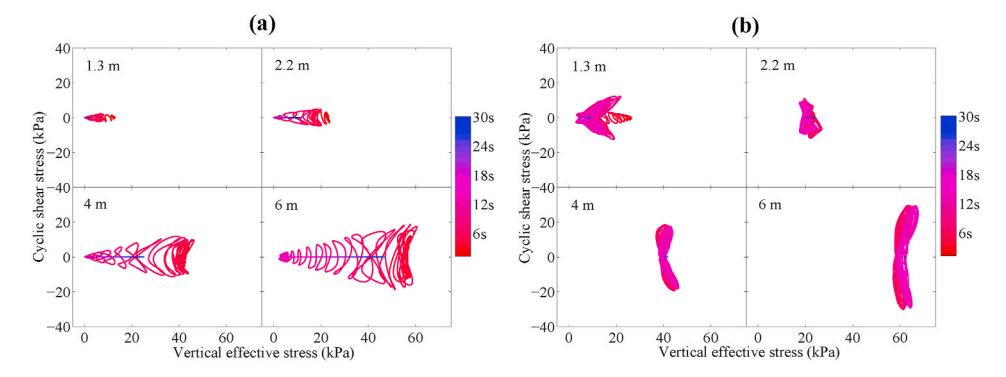


Fig. 14. Time histories of effective stress path at selected depths for: a) loose level deposit and b) dense level deposit.

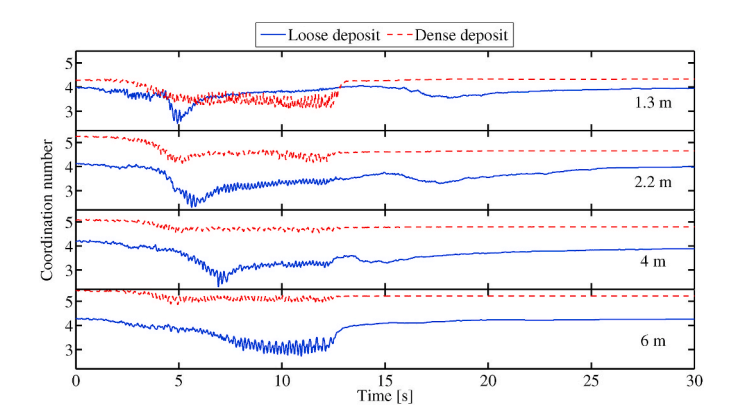
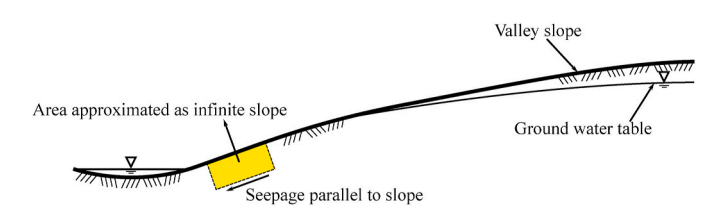


Fig. 15. Time histories of coordination number at selected depths.



**Fig. 16.** A schematic view of seepage below a natural slope and area approximated as an infinite slope.

the other was dense and not expected to liquefy. In order to reduce the size of the model and bring the number of particles to a manageable size, the model was subjected to a high g-level similar to that used in geotechnical centrifuge physical testing. By following centrifuge testing scaling laws [89], the linear and temporal dimensions in the model are scaled down by N compared to the prototype, where N is the gravitational acceleration multiplier. Additionally, periodic boundaries were employed at all lateral sides of the model for both DEM and SPH particles to simulate a repeated pattern in an infinite medium with a limited number of particles (Fig. 2). The lower boundary, which represents the bedrock, was modeled by a rigid wall in DEM and by a no-slip, impermeable boundary in SPH. The seismic excitations were applied to the fluid and solid phases through the base boundaries.

The modeled 5.85 m high sand layer had lateral dimensions of 1.44 m by 1.44 m (all in prototype units) and was created using a particle size range of 1.5 mm–2.5 mm, which is close to the coarse sand grain size. The particles were generated in a relatively large space and allowed to settle under the high gravitational field of 30g. In addition, rolling friction was introduced between spherical particles to compensate for their non-irregular shapes and prevent excessive relative rotations. The loose sand layer was determined to have an average porosity and

saturated unit weight of around 44% and  $18.9 \, \mathrm{kN/m^3}$ , respectively. For the dense layer, the average porosity and saturated unit weight were, respectively, around 38.5% and  $19.8 \, \mathrm{kN/m^3}$ .

The 1 m thick (in prototype units) impermeable crust was created using spherical particles glued together by parallel bonds. The crust was placed on the sand layer and the whole system was allowed to reach equilibrium. The impermeable layer had a saturated unit weight of around 20 kN/m³. In order to make this layer completely impervious, two layers of SPH particles were placed at the locations of the DEM particles composing the bottom part of the crust. These SPH particles move with their DEM counterparts and each pair can be considered as a single hybrid particle. The hybrid particles interact with surrounding DEM particles through contact forces and receive hydrodynamic forces from other fluid particles. This method is commonly used in fluid-structure interaction problems using SPH [67].

The fluid domain had the same lateral dimensions of the periodic space and was modeled using SPH particles with initial spacing and kernel radius of, respectively, 4 mm and 6 mm. The 3D view of the saturated loose deposit with the crust is shown in Fig. 2. A high prototype fluid viscosity of 0.02 Pa.s was employed to account for the high gravitational field of 30g and the relatively large particle sizes. For the prototype fluid viscosity of 0.02 Pa.s and the employed particle size range, the initial permeability of the sand layer was estimated to be 2.9 mm/s (same order of coarse sand permeability when saturated with water) using the Kozeny-Carmen equation [90] for the loose deposit and 1.64 mm/s for the dense deposit. A summary of parameters used in the conducted simulations is provided in Table 1. The deposits were subjected to a dynamic excitation that was introduced as a prescribed velocity time history to the base wall that would produce a sinusoidal motion with a maximum amplitude of 0.25g and a frequency of 3Hz. The sinusoidal input signal gradually increases until it reaches the maximum acceleration amplitude at 4.5 s, where it remains constant for an additional 7.5 s before it gradually decreases to zero at 13 s. During the simulations, averaged particle velocity, stress and strain rate tensors, porosity and coordination number were monitored from the PFC3D environment using spherical volumes (sufficiently large to include hundreds of particles inside) positioned along the depth of the deposits. Fluid pressure and velocity at the corresponding locations of the averaging volumes were retrieved from the SPH analysis. Results of conducted simulations are presented in the following sections exclusively in prototype units.

# 3.1. Response of level deposits

Before discussing the response of sloping deposits, it was worth examining the behavior of the less complex setup of a level deposit composed of a sand layer overlain by an impermeable crust. The most anticipated result of these simulations was the ability of the proposed computational framework to capture the formation of a water interlayer at the interface between the crust and the underlying soil. Fig. 3 shows

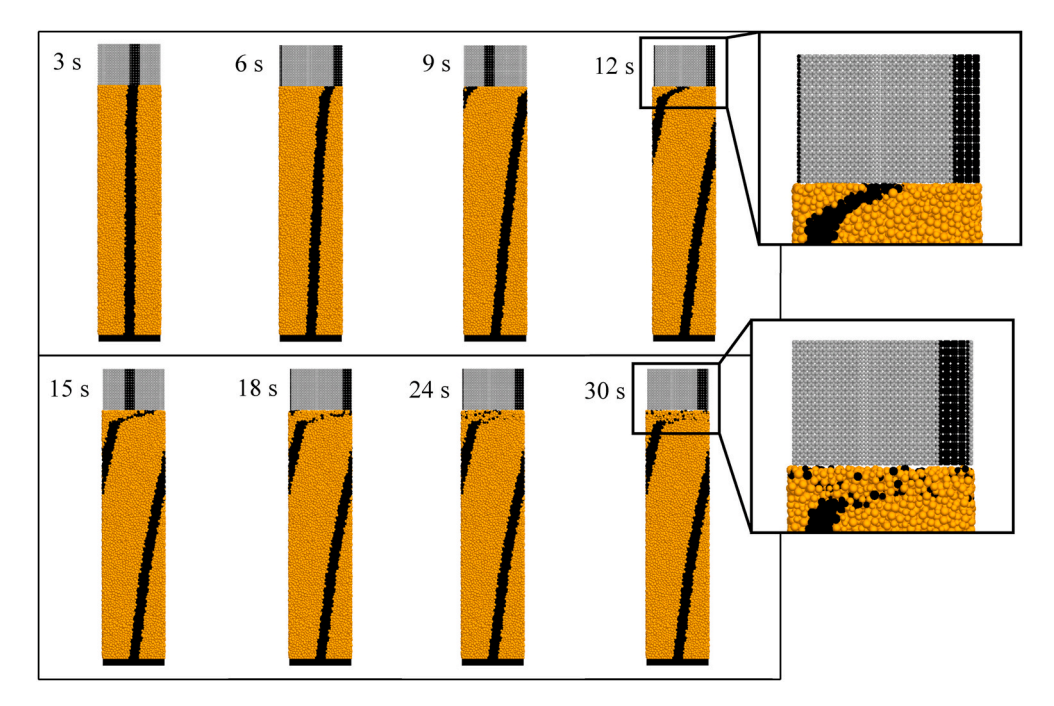


Fig. 17. Snapshots of lateral displacement profiles in the loose sloping deposit.

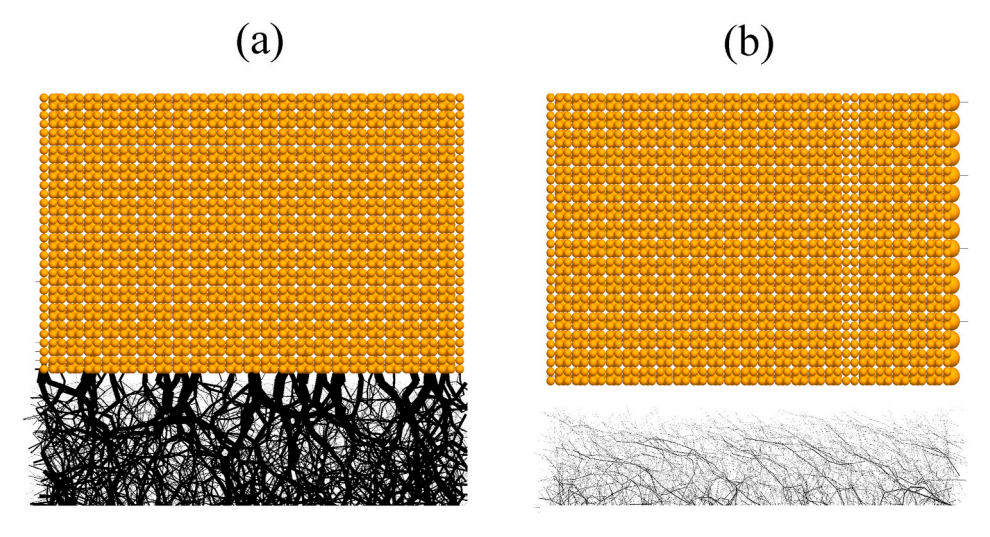


Fig. 18. Snapshots of contact chains at the interface between soil and crust: (a) Before shaking, and (b) At end of simulation.

that indeed the loose deposit experienced the formation of a water film at the interface. To the best of the authors' knowledge, this is the first time a computational technique captures the formation of a water film in such geotechnical systems. The size of the gap between the crust and the underlying soil was about 9 cm by the end of the simulation. The formation of a water film is expected based on the theoretical analysis of Malvick et al. [9] and was observed experimentally by Kokusho [16]. It should be noted, however, that several factors affect the physical formation of the water film in real soil deposits. For instance, the potential cracking of the crust could relieve the pressure and lead to no formation of the water film. The dense deposit did not exhibit any separation between the crust and the underlying soil.

Liquefaction in level deposits is generally characterized by the excess pore pressure ratio (ratio of excess pore-water pressure to the initial vertical effective stress) approaching the magnitude of one. At this point, the shaking-induced pressure has counterbalanced the initial effective stress, leading to a complete loss of soil strength. Fig. 4 shows the excess pore pressure time histories for the loose and dense deposits at several

depth locations below the crust. The loose deposit exhibited the familiar patterns of pore-pressure buildup and liquefaction taking place near the surface and propagating downward as shaking progressed. Almost the entire depth of the loose deposit liquefied as the pore pressure ratio approached the value of one at all depth locations. The dense deposit, on the other hand, showed instantaneous pore-pressure buildup near the surface that was not sustained. Pore pressure went down to zero following the end of shaking in the case of the dense deposit. Porepressure development post shaking in the loose deposit, however, showed a sustained value higher than zero until the end of the simulation (Fig. 5). This value corresponds to the effective stress due to the weight of the crust layer that was essentially being carried by water and lost contact with the underlying soil layer due to the development of the water film (Fig. 3). The change in vertical effective stresses along the depth of the loose sand deposit before shaking and at the end of the simulation is shown in Fig. 6. The two fitting straight lines are almost parallel with an offset equal to the stress induced by the effective weigh of the crust layer.

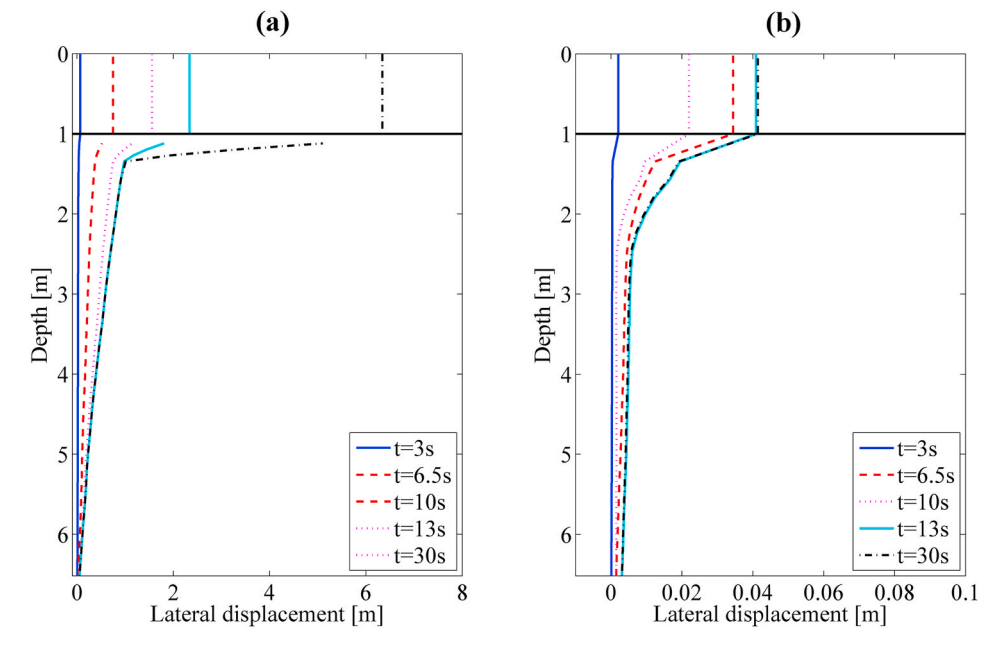


Fig. 19. Lateral displacement profiles at selected time instants for: a) loose sloping deposit, and b) dense sloping deposit.

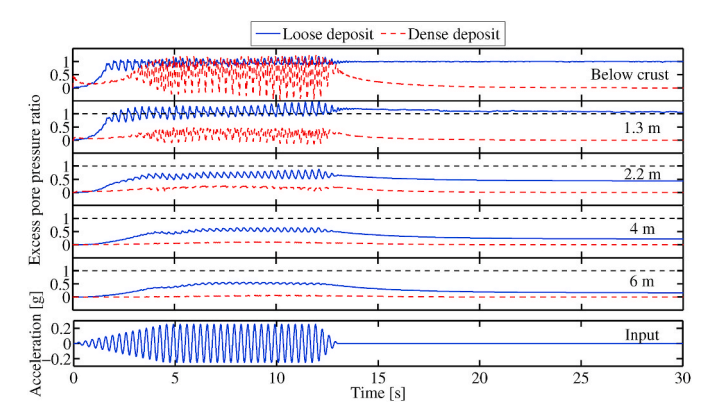


Fig. 20. Time histories of excess pore pressure ratio at selected depth locations.

Profiles of excess pore pressure along the depth of the loose deposit are shown in Fig. 7. Pore-pressure quickly jumped to a value equal to magnitude of the effective stress due to the weight of the crust layer (the t=3 s instant). As shaking continued, pore-pressure gradually increased and reached the initial effective stress starting from the top of the sand layer and propagating downwards. After the end of shaking, pore pressure gradually dissipated from the bottom depth location towards the surface. By the 24 s time mark, there was no further pore-pressure dissipation but the pore pressure profile remained at a constant value equal to the stresses induced by the effective weight of the crust (about  $10~\mathrm{kPa}$ ).

In the presented SPH-DEM model, the coupling between the phases is explicitly evaluated through a drag force exerted by the fluid on the solid particles. Conceptually, when this drag force completely counterbalances the weight of the particle, the soil grains will be essentially floating or in other words, liquefied. The average drag force applied on solid particles normalized by the weight of the particles was computed at different depth locations along the loose and dense deposits (Fig. 8). Almost all depths of the loose deposit (except for the location near the base) experienced a normalized drag force value of one, indicating liquefaction. The crust layer overlying the liquefied sand remained floating for the rest of the simulation. Only the shallow depth of 1.3 m in the dense deposit showed instantaneous normalized drag force of one.

The drag force remained constant and equal to the buoyant magnitude for the entire simulation for the deeper parts of the dense deposit.

Pore pressure generation during earthquake shaking is strongly correlated to volumetric strains. Densification (or volumetric contraction) squeezes water inside the pores and leads to water pressure development and flow. Fig. 9 shows the evolution of volumetric strains along the depth of the loose deposit. Overall, the deposit experienced contraction along its depth with higher contraction values observed to take place near the top of the deposit followed by contraction at deeper depth locations. After the end of shaking (around the 12 s instant), there was no further changes in volumetric strains for the remainder of the simulation. Fig. 10 shows the variation of porosity with depth for the loose and dense deposits. The loose deposit experienced reduction in volume along its depth by the end of shaking (Fig. 10a and b). No further significant changes took place from the end shaking until the end of the simulation (Fig. 10b and c). The dense deposit remained practically with the same porosity distribution throughout the simulation (Fig. 10d, e, f).

One of the advantages of the utilized coupled SPH-DEM approach is the ability to monitor fluid motion. Fig. 11 depicts the vertical fluid velocity (relative to average particle velocity) profiles along the depth of the loose deposit. After about 4.8 s, fluid flow was essentially upward and continued to move towards the surface post shaking (during the dissipation phase). Fluid motion almost came to a stop by the end of the simulation. Average solid particle velocities were monitored throughout the simulations and were used to obtain the acceleration time histories shown in Fig. 12. In the case of the loose deposit, there was an initial phase of motion amplification before liquefaction of the sand layer took place at around 5 s near the surface and propagated downwards (Fig. 12a). During that phase of motion amplification, the magnitude of the amplification factor was about 1.67. It could be seen that the acceleration amplitude almost vanished at the 4 m depth around 7 s (Fig. 12a). The formation of the water film at the interface between the crust and the underlying soil prevented any transmission of motion to the crust layer. There was no sign of motion degradation in the dense deposit. In fact, motion amplification was observed with an amplification factor reaching a magnitude of about 3.15 at the crust (Fig. 12b).

Cyclic shear stress-strain histories are shown in Fig. 13. As expected (and in agreement with observations from excess pore pressure and acceleration time histories), there was near-complete loss of stiffness as liquefaction occurred accompanied with large shear strains in the case of

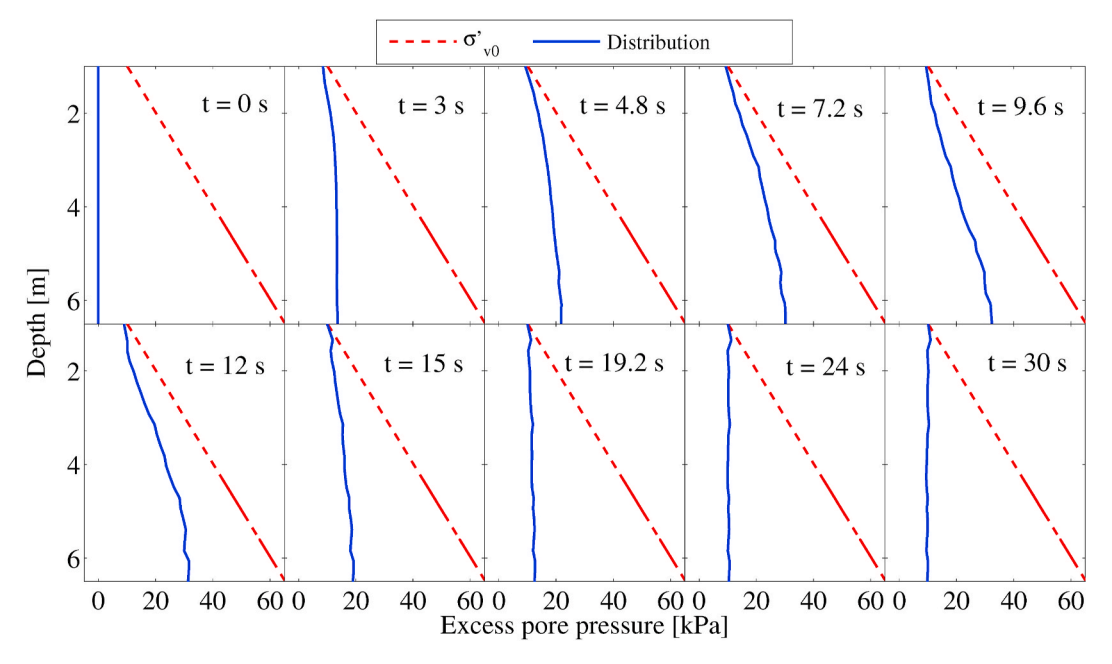


Fig. 21. Excess pore pressure profiles at selected time instants for the loose sloping deposit.

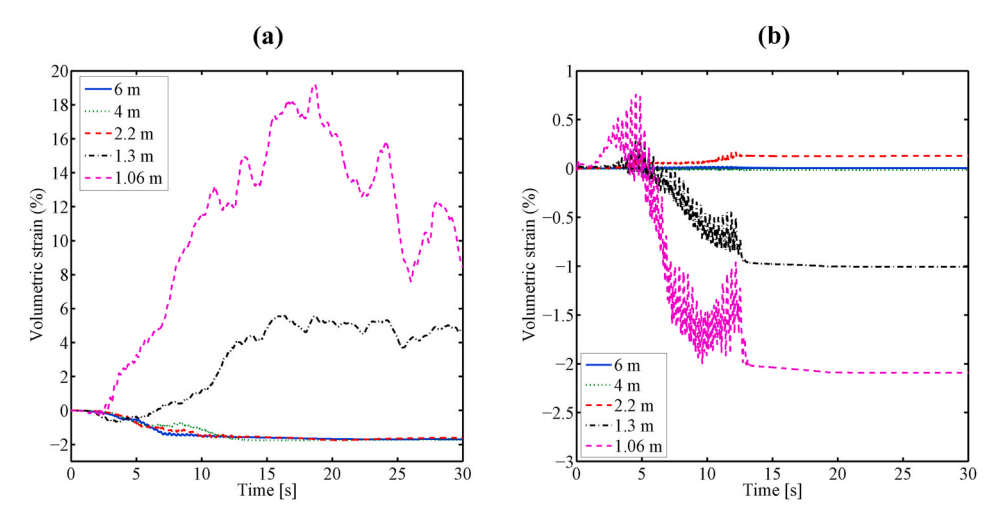


Fig. 22. Time histories of volumetric strain at selected depths for: a) loose sloping deposit, and b) dense sloping deposit.

the loose deposit (Fig. 13a). Except for the location near the surface of the dense deposit that experienced large strains and stiffness degradation, the dense deposit maintained its stiffness and experienced much smaller shear strain levels especially at deeper depth locations (Fig. 13b). The effective stress paths are shown in Fig. 14 for the loose and dense deposits. The Figure shows that the vertical effective stress essentially vanished as the loose deposit liquefied. It also shows that the vertical effective stress recovered to a value less than the initial value by the end of the simulation. The difference being approximately the effective stress resulting from the weight of the crust layer that was completely carried by water (Fig. 14a). Only the shallow depth of 1.3 m experienced instantaneous reduction in effective stress in the case of the dense deposit. Signs of dilation marked by the increase in vertical effective stresses and associated shear stresses could be observed at that location (Fig. 14b).

Modeling granular materials based on micromechanical considerations allows the investigation of microscale response mechanisms. For instance, the coordination number (defined as the average number of contacts per particle in the packing) represents means to characterize the stability of a packing of frictional spheres. The higher the

coordination number, the more stable the packing is as it leads to a stronger network chain of interparticle contacts. A low coordination number (lower than 4 for frictional spheres [91]) indicates the packing is unstable. Fig. 15 shows that the coordination number fell below the value of 4 at all depth locations in the loose deposit, while only the 1.3 m location experienced such reduction in the dense deposit. Post shaking, the loose deposit was marginally stable.

# 3.2. Response of sloping deposits

After verifying the ability of the presented SPH-DEM framework to capture the formation of the water film at the crust-granular soil interface in level loose deposits, simulations of sloping deposits were performed. The same level deposits described in the previous Section were used to model infinite slopes with seepage parallel to slope by introducing a component of gravity parallel to slope that corresponds to a  $5^{\circ}$  slope, while keeping fluid flow parallel to the slope. That is, the DEM and SPH particles were subjected to a gravitational acceleration which deviates from the vertical axis by  $5^{\circ}$ . The slopes had a safety factor higher than 3 against slope instability under static conditions. The

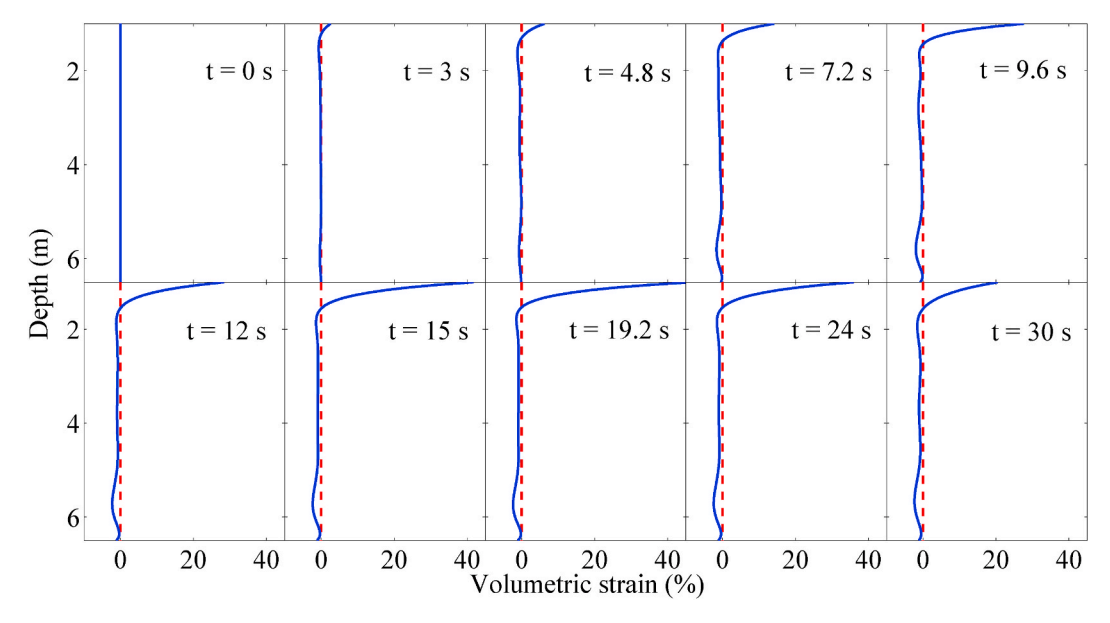


Fig. 23. Volumetric strain profiles at selected time instants for the loose sloping deposit.

saturated infinite slope with seepage parallel to slope is an approximation to the part of the slope shown in Fig. 16. As discussed below, when subjected to the strong shaking amplitude of 0.25 g, the loose sloping deposit showed signs of flow liquefaction and instability while the dense deposit did not liquefy.

As in the case of the level deposit, snapshots of the loose sloping deposit at different time instants throughout the simulation are shown in Fig. 17. Separation between the motion of the crust and the underlying layer started around the 6 s mark. This separation was observed in the centrifuge tests of lateral spreading reported by Kamai [3]. The crust was clearly displacing laterally at a much larger magnitude than the underlying soil. A small gap between the crust and the underlying soil formed by the end of shaking (around the 12 s time instant). The separation between the soil and the overlying crust is confirmed by the contact chains at the interface (Fig. 18). Before shaking, the weight of the crust layer was carried by the underlying soil and the chain network had a large magnitude (Fig. 18a). As shaking progressed and water flowed towards the surface, flow liquefaction took place (as discussed later on), the contact forces at the interface vanished and the crust was completely carried by water (Fig. 18b). This led to the crust sliding downslope on a water film under the effect of the gravity component in the direction parallel to slope. Flow failure of a sand layer confined to about 0.3 m in thickness at the interface could be seen continuing post shaking after the 15 s mark. Within that thickness, the soil was fluidized and not deforming as a continuum anymore (see the snapshots at 18, 24 and 30 s in Fig. 17). The magnitude of the lateral displacement of the crust by the end of shaking was about 2.4 m (Fig. 19a). There was a discontinuity in the displacement profiles starting after about 6 s of shaking. The crust layer continued to displace laterally following the end shaking, reaching a displacement of about 6.3 m by the end of the simulation (t = 30 s in Fig. 19a). A thin sand layer below the crust of a thickness of about 0.3 m also experienced significant deformation as high as 5.2 m. In theory, those two locations will continue to displace downslope indefinitely. Below that top thin layer, the deposit stopped deforming laterally post shaking and reached a lateral displacement of about 1.8 m. The lateral displacement of the crust on top of the dense sand was about 0.04 m by the end of shaking and the crust and the underlying soil did not displace any further post shaking (Fig. 19b).

Buildup in pore pressure and reaching a pore-pressure ratio close to the value of one was only observed in the depth immediately under the crust (Fig. 20). This ratio remained equal to one for the remainder of the simulation (about 17 s post shaking) as in the level loose deposit. For the

deeper depth locations, the pore pressure ratio stabilized at the value corresponding to the pressure induced by the effective weight of the crust layer. The dense sloping deposit showed instantaneous pore-pressure ratio of one immediately below crust but pore-pressure ratio turned back to zero within 2 s after the end of shaking. For most of the depth along the dense deposit, the pore-pressure ratio barely changed. Note that post shaking, the excess pore pressure in the loose deposit maintained a magnitude equal to the stress induced by the effective weight of the crust, indicating the formation of a thin water film and the transmission of the weight of the crust to be carried entirely by porewater similar to the case of the level loose deposit (Fig. 21).

Excess pore pressure profiles at different time instants along the depth of the loose deposit confirm that shaking-induced pore pressure was less than the initial effective stress for most of the depth (Fig. 21). This is significantly different than the behavior of the same deposit without a slope where excess pore pressure approached the initial magnitude of the vertical effective stress along most of the depth (Fig. 7). This difference in response is explained by exploring volumetric strains and void redistribution. In order to better capture the volumetric strains, special code was written to evaluate the strain rate at the 1.06 m depth location to ensure that the averaged particle velocities (which are needed to evaluate the strain rate tensor) do not include the particles in the crust layer. Volumetric strain time histories are shown in Fig. 22 for the loose and dense sloping deposits. Initially, all the depth locations along the loose deposit experienced contraction for the first 2.5 s of shaking (Fig. 22a). During this period, buildup in excess pore pressure took place that was sufficient to liquefy the surface layers of the loose deposit (Fig. 21). Once liquefied, the surface of the loose deposit showed significant dilation that started at about 3 s from the start of shaking and reached values as high as 18%. This was followed by the 1.3 m depth location that experienced a dilative volumetric strain of about 5% (Fig. 22a). The maximum dilatation at both locations took place after the end of shaking. Below 1.3 m, the loose deposit experienced contraction in the order of 2%. In the case of the dense deposit, those two top depth locations initially experienced dilation less than 1% over the first 5 s before turning into contraction for the rest of the simulation. Fig. 23 shows a clearer picture of the progressive increase in volume near the interface with the crust that started early in the shaking and reached values as high as 40%. The pattern of volumetric strains in Fig. 23 agree with the centrifuge test results reported by Boulanger et al. [2] and Malvick et al. [9]. It should be noted, however, that the magnitude of volumetric strain near the surface observed here are much higher than

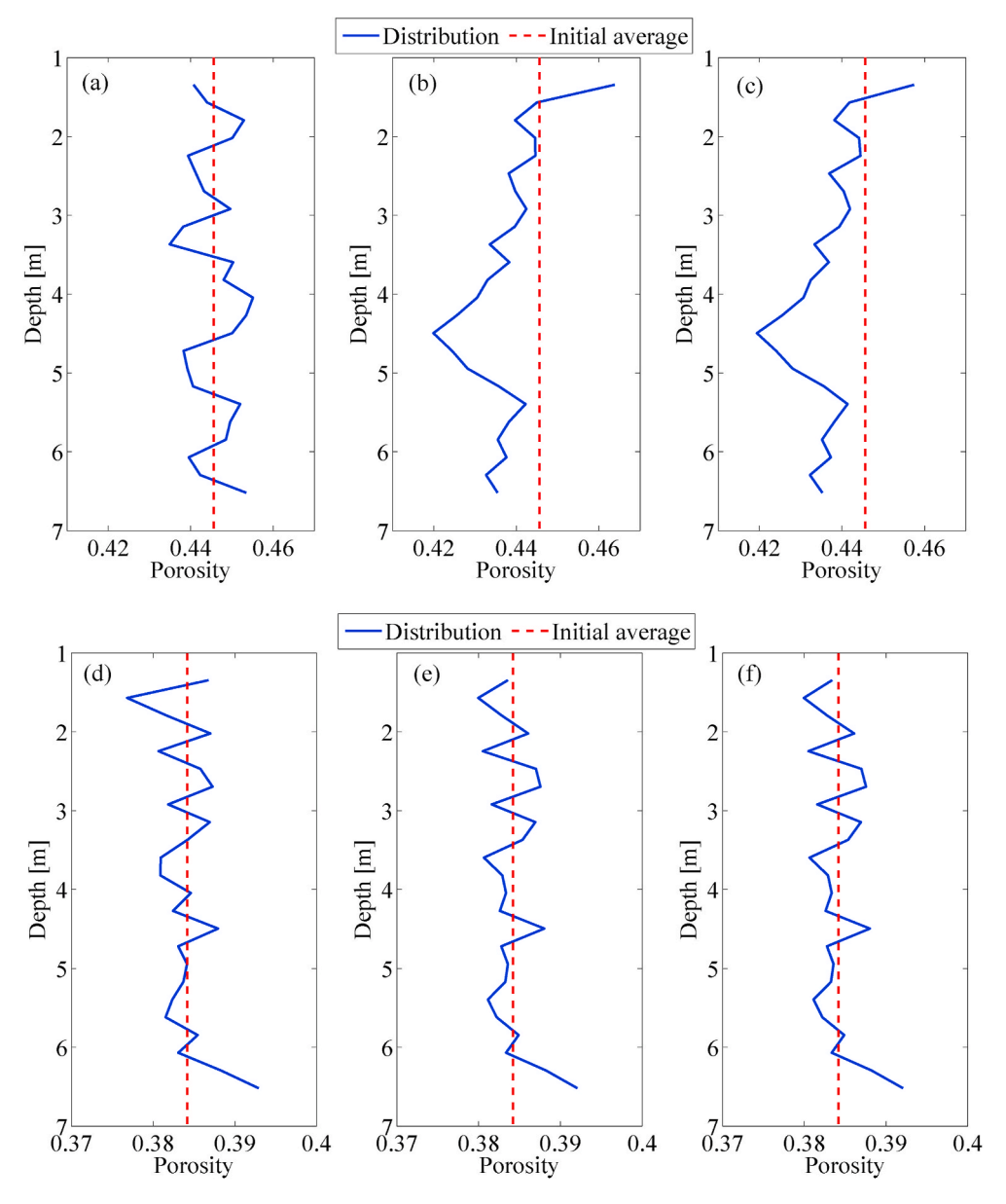


Fig. 24. Porosity profiles for the loose sloping deposit at: a) start of simulation, b) end of shaking and c) end of simulation as well as the dense sloping deposit at: d) start of simulation, e) end of shaking and f) end of simulation.

those observed in the centrifuge tests. As noted by Malvick et al. [9], the magnitude of volumetric strain is influenced by the shaking intensity and duration as well as soil permeability and relative density.

Void redistribution is confirmed by looking at the porosity profiles with depth shown in Fig. 24. Before shaking, the porosity distribution was fairly uniform along the depth (Fig. 24a). By the end of shaking, significant contraction could be observed along the locations below the 1.3 m depth. The surface of the loose sand, however, experienced significant increase in void space (Fig. 24b). The distribution of void space remained almost the same post shaking and until the end of the simulation (Fig. 24c). The dense deposit did not show any significant changes in porosity throughout the simulation (Fig. 24d, e, and f).

The increase in volume near the surface of loose sand deposit attracts water flow towards the surface, thereby releasing the pressure from the deeper depth locations. Relative fluid-particle velocity profiles are shown in Fig. 25 and confirm water flow patterns. It should be noted that while the patterns in Fig. 25 are similar to the ones observed previously in the case of the loose level deposit (Fig. 11), the mechanism behind pore-pressure generation and water flow is completely different. In the

level deposit, pore-pressure generation was in response to the contraction taking place along the deposit. In the case of the sloping deposit, pore-pressure initially developed due to contraction but flow was facilitated by the dilation taking place near the surface.

Unlike the loose level deposit where accelerations diminished along most of the liquefied depth, the accelerations in the loose sloping deposit did not vanish (Fig. 26a). Small amplitude acceleration was transmitted to the crust. Negative spikes could be observed at the 1.3 m depth location towards the end of shaking. The dense sloping deposit showed motion amplification (Fig. 26b) as in the case of the level one. Plots of the average lateral velocity at different depth locations are shown in Fig. 27. It could be seen that crust in the case of the loose deposit underwent nearly constant velocity downslope post shaking at a magnitude of about 0.25 m/s (Fig. 27a). The dense deposit came to a complete stop following the end of shaking (Fig. 27b).

The normalized drag forces in the case of the sloping deposits are shown in Fig. 28. The normalized drag forces show that the top 4 m have experienced instability caused by normalized drag forces approaching a value close to one. As in the case of the level dense deposit, the

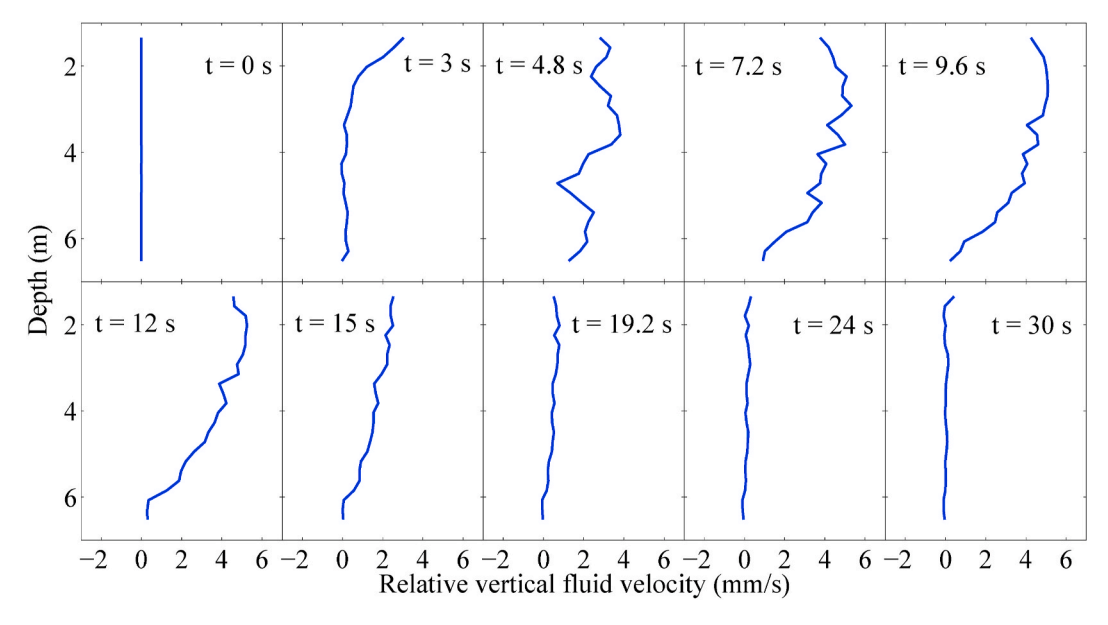


Fig. 25. Vertical fluid velocity profiles at selected time instants for the loose sloping deposit.

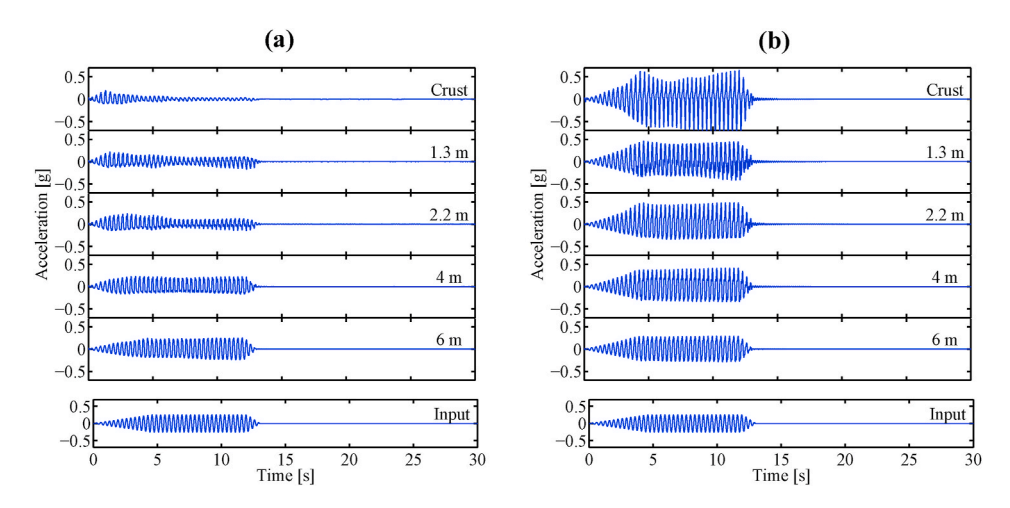


Fig. 26. Time histories of average horizontal acceleration at selected depths for: a) loose sloping deposit, and b) dense sloping deposit.

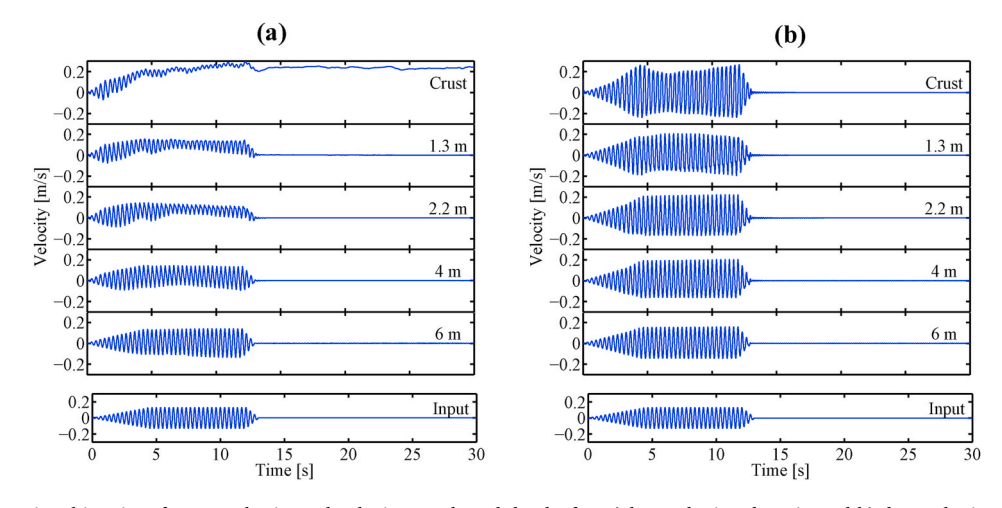


Fig. 27. Time histories of average horizontal velocity at selected depths for: a) loose sloping deposit, and b) dense sloping deposit.

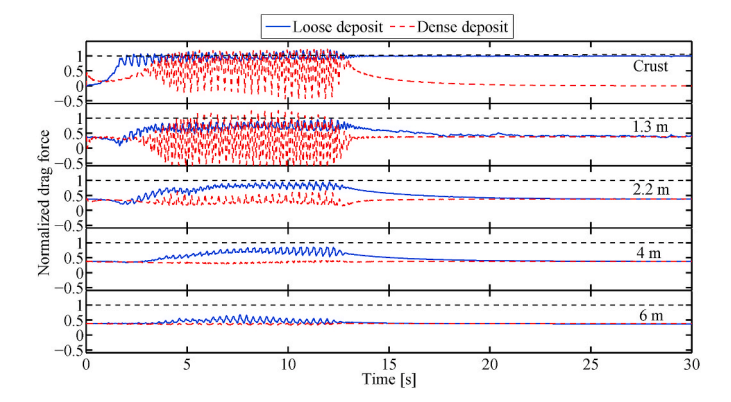


Fig. 28. Time histories of vertical fluid drag force normalized by the average particle weight at selected depths.

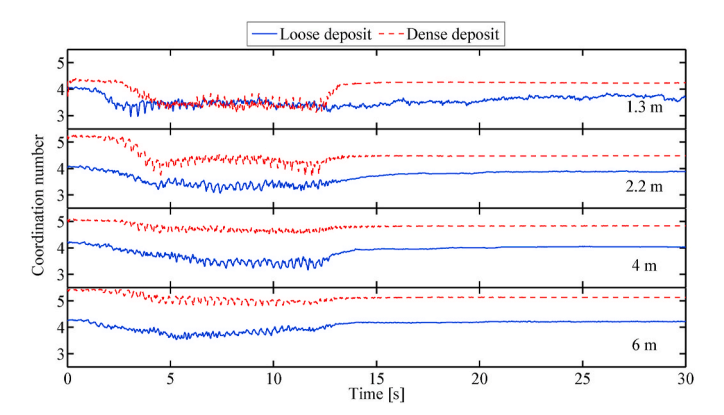
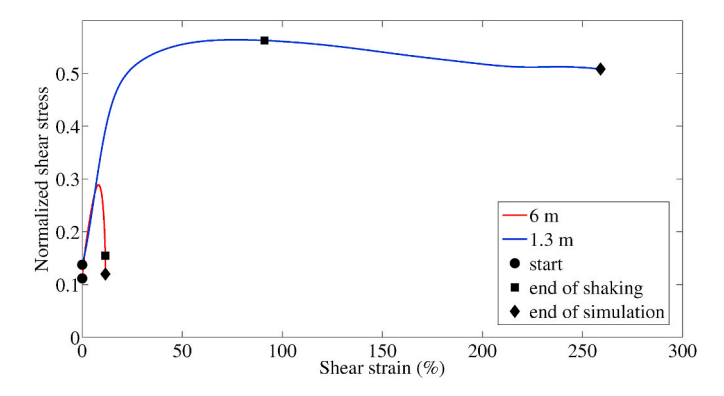


Fig. 29. Time histories of coordination number at selected depths.



 $\textbf{Fig. 30.} \ \ Plot \ \ of \ normalized \ \ shear \ \ stress \ \ versus \ \ shear \ \ strain \ \ for \ \ the \ \ loose \ \ sloping \ \ deposit.$ 

normalized drag forces in the dense sloping deposit remained virtually unchanged except for the location near the surface where it oscillated in response to cycles of dilation and contraction that occurred at that location. Time histories of the coordination number (Fig. 29) confirm that the entire loose deposit was unstable during shaking. The coordination number at the 1.3 m depth location remained at a value below 4 post shaking, indicating sustained instability until the end of the simulation. Only the 1.3 m depth location in the dense deposit showed instability during shaking but recovered once shaking stopped.

In order to examine the mechanisms illustrated in Fig. 1, several aspects of the response of the loose sloping deposit were processed at two key points, one near the surface (just below the crust) and the other near the base of the deposit. Fig. 30 shows the evolution of the

normalized shear stress at those two locations with shear strain. The computed shear stress at a certain location was normalized by the corresponding vertical effective stress and the response was filtered to obtain the noncyclic part. The behavior is somewhat similar to the schematic in Fig. 1c. The top location at the 1.3 m depth shows a peak in strength followed by softening and eventually reaches a plateau associated with the residual shear strength of the soil. The corresponding peak friction angle is  $29.3^{\circ}$  and residual friction angle is  $26.6^{\circ}$ , which are typical values for rounded loose sand. Note that the shear strain continued to accumulate (flow) significantly post shaking near the surface of the deposit.

Fig. 31 shows several response mechanisms at the shallow and deep depth locations of the loose sloping deposit. The void ratio vs. vertical effective stress (Fig. 31a) shows a pattern similar to Fig. 1b. Near the surface, the void ratio underwent an initial decrease followed by an increase until end of shaking (Fig. 31a). Near the base of the deposit, there was a small contraction after undergoing no volume change at the initial stage of shaking, and there was no change in void ratio post shaking. The volumetric strain near the surface shows that after an initial contraction near the surface, that location experienced significant increase in volume that kept increasing until the end of shaking (Fig. 31b). Post shaking, there was little further increase in volume. At the 6 m depth location, the behavior was contraction during shaking and no further volume change occurred once shaking stopped. The shear stress-strain history near the surface shows diminishing shear stress amplitude as shaking progressed in response to pore-pressure development (Fig. 31c). Again, large accumulation of shear strain took place by the end of shaking (in the order of about 90%) and continued post shaking reaching strains as high as about 270%. At the deeper depth of 6 m, the accumulated shear strain by the end of shaking was about 20% and there was no further accumulation of strains post shaking. It is worth noting that one could argue that while flow liquefaction and associated large deformation was clearly observed near the surface of the deposit, experiencing 20% shear strain is by far higher than any acceptable strain levels in practice. Therefore, the whole deposit could be considered unstable as discussed earlier from looking at coordination number and normalized drag forces. The effective stress path at the two depth locations is shown in Fig. 31d, along with the Mohr-Coulomb (M-C) failure envelopes obtained from Fig. 30. The stress path at the shallow depth of 1.3 m, shows that by the end of shaking and through the end of the simulation, the stress moved along the residual stress failure envelope. At the deeper depth location of 6 m, the shear stress instantaneously approached the residual strength of the soil at that location. At both locations, the vertical effective stress at the end of the simulation was less than that at the start of shaking by an offset value equal to the stress induced by the effective weight of the crust. These observations are in agreement (conceptually) with the behavior sketched in Fig. 1d.

# 4. Conclusions

A coupled SPH-DEM model was utilized herein to model potential flow liquefaction of saturated granular soils overlain by an impermeable crust layer. Simulations of loose and dense level and sloping deposits were performed. In the case of level deposits, results showed that the dense deposit, as expected, did not liquefy and showed motion amplification. However, the loose deposit liquefied due to contraction of void space that led to pore pressure development and subsequent reduction in effective stress. A water film visibly formed at the interface between the top crust layer and the underlying liquefied soil. Liquefaction of the loose level deposit was marked by vanishing acceleration records, excess pore pressure ratios approaching the value of one, normalized drag forces that counterbalance the weight of the solid particles, and coordination numbers that fell below the minimum value needed to maintain a stable packing. During shaking, water flow towards the surface was observed in response to local contraction along the depth of loose deposit.

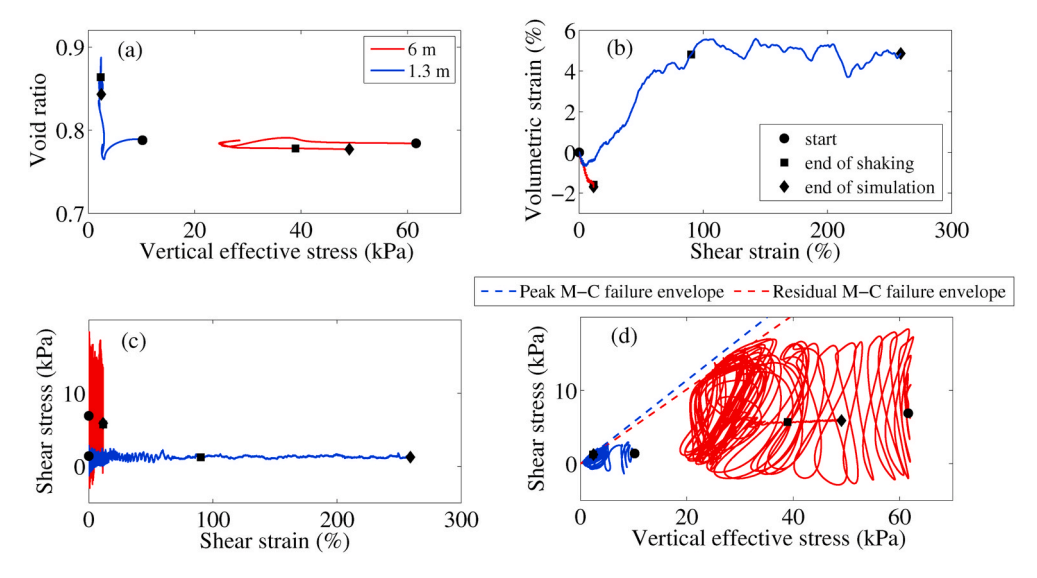


Fig. 31. Soil responses near the top and bottom of the liquefiable layer for the loose sloping deposit.

The dense sloping deposit did not liquefy and showed very little lateral deformation. On the other hand, the loose sloping deposit liquefied and showed several mechanisms that have been hypothesized about the behavior of such systems for several decades and observed in published experimental work on liquefaction-induced flow failure and void redistribution. Results of performed simulations revealed that the loose deposit initially contracted leading to buildup in pore-pressure that quickly formed a gradient sufficient to liquefy a thin layer (in the order of 0.3 m) below the crust because of the contrasting permeability with the crust layer. Once liquefied, it moved downslope and experienced dilation that facilitated water flow towards the surface and relieved the pressure at deeper depth locations. As shaking continued, deeper depth locations underwent further contraction leading to a clear void redistribution along the depth of the deposit. Flow liquefaction of the thin layer was marked by high pore pressure ratio, large lateral displacement (in the order of meters) that continued post shaking. diminishing shear stress and vertical effective stress as well as unstable particle packing reflected by a small value of coordination number. At deeper depth locations, shear strains were in the order of 20% and coordination numbers were low, indicating that the majority of the depth of the loose deposit was unstable during shaking. However, post shaking the depths below the thin layer that experienced flow failure stopped accumulating lateral displacement. While not as visible as in the case of the level loose deposit, evidence of a water interlayer was observed as the top crust moved downslope at almost a constant velocity post shaking. Additionally, the stress induced by the effective weight of the crust layer completely transferred to the fluid.

The presented SPH-DEM framework is able to capture the complicated behavior of soil liquefaction and flow failure with relatively simple assumptions and a small number of parameters. A major strength of this framework is its seamless nature in the sense that the input parameters are physically interpretable and do not change with the change of the simulated deposit. As computational resources and parallel computing advance, the implementation of the presented technique would become more and more popular for numerical modeling of geotechnical systems.

## CRediT authorship contribution statement

**Usama El Shamy:** Conceptualization, Methodology, Investigation, Supervision, Writing – original draft. **Saman Farzi Sizkow:** Software, Formal analysis, Data curation, Visualization, Writing – review & editing.

## **Declaration of competing interest**

The authors declare that they have no known competing financial interests or personal relationships that could have appeared to influence the work reported in this paper.

# Acknowledgement

This research was partially supported by the US Army Corps of Engineers Engineer Research and Development Center, grant number W9132V-13-C-0004 and the National Science Foundation award number CMMI-1728612. These supports are gratefully acknowledged.

# References

- National Research Council, et al. Liquefaction of soils during earthquakes. Committee on Earthquake Engineering; 1985.
- [2] Rw Boulanger R Kamai, Ziotopoulou K. Liquefaction induced strength loss and deformation: simulation and design. Bull Earthq Eng 2014;12(3):1107–28.
- [3] Kamai R. Liquefaction-induced shear strain localization processes in layered soil profiles. Davis: University of California; 2011.
- [4] Malvick EJ, Kutter BL, Boulanger RW. Postshaking shear strain localization in a centrifuge model of a saturated sand slope. J Geotech Geoenviron Eng 2008;134 (2):164–74.
- [5] Whitman Robert V. On liquefaction. In: International conference on soil mechanics and foundation engineering, vol. 11; 1985. p. 1923–6.
- [6] Boulanger RW, Truman SP. Void redistribution in sand under post-earthquake loading. Can Geotech J 1996;33(5):829–34.
- [7] Sento N, Kazama M, Uzuoka R, Ohmura H, Ishimaru M. Possibility of postliquefaction flow failure due to seepage. J Geotech Geoenviron Eng 2004;130 (7):707–16.
- [8] Yoshimine M, Nishizaki H, Amano K, Hosono Y. Flow deformation of liquefied sand under constant shear load and its application to analysis of flow slide of infinite slope. Soil Dynam Earthq Eng 2006;26(2–4):253–64.
- [9] Malvick EJ, Kutter BL, Boulanger RW, Kulasingam R. Shear localization due to liquefaction-induced void redistribution in a layered infinite slope. J Geotech Geoenviron Eng 2006;132(10):1293–303.
- [10] Liu H, Qiao T. Liquefaction potential of saturated sand deposits underlying foundation of structure. In: Proceedings of the 8th world conference on earthquake engineering, san francisco, calif; 1984. p. 21–8.
- [11] Elgamal AW, Dobry R, Adalier K. Study of effect of clay layers on liquefaction of sand deposits using small-scale models. In: Proc., 2nd US-Japan workshop on liquefaction, large ground deformation and their effects on lifelines; 1989. p. 233-45.
- [12] Dobry R, Liu L. Centrifuge modeling of soil liquefaction. In: Proc., 10th world conf. On earthquake engineering. Spain: International Association for Earthquake Engineering (IAEE) Madrid; 1992. p. 6801–9.
- [13] Fiegel GL, Kutter BL. Liquefaction mechanism for layered soils. J. Geotech. Eng. 1994;120(4):737–55.
- [14] Uchida K, Vaid YP. Sand behaviour under strain path control. In: International conference on soil mechanics and foundation engineering; 1994. p. 17–20.

- [15] Vaid YP, Eliadorani A. Instability and liquefaction of granular soils under undrained and partially drained states. Can Geotech J 1998;35(6):1053–62.
- [16] Kokusho T. Water film in liquefied sand and its effect on lateral spread. J Geotech Geoenviron Eng 1999;125(10):817–26.
- [17] Kokusho T. Mechanism for water film generation and lateral flow in liquefied sand layer. Soils Found 2000;40(5):99–111.
- [18] Tokimatsu K, Taya Y, Zhang JM. Effects of pore water redistribution on postliquefaction deformation of sands. In: International conference on soil mechanics and geotechnical engineering; 2001. p. 289–92.
- [19] Kokusho T. Current state of research on flow failure considering void redistribution in liquefied deposits. Soil Dynam Earthq Eng 2003;23(7):585-603.
- [20] Kulasingam R, Malvick EJ, Boulanger RW, Kutter BL. Strength loss and localization at silt interlayers in slopes of liquefied sand. J Geotech Geoenviron Eng 2004;130 (11):1192–202.
- [21] Kamai R, Boulanger RW. Characterizing localization processes during liquefaction using inverse analyses of instrumentation arrays. 2010.
- [22] Balakrishnan A. Liquefaction remediation at a bridge site. 2000.
- [23] Yoshida N, Finn WDL. Simulation of liquefaction beneath an impermeable surface layer. Soil Dynam Earthq Eng 2000;19(5):333–8.
- [24] Yang Z, Elgamal A. Influence of permeability on liquefaction-induced shear deformation. J Eng Mech 2002;128(7):720–9.
- [25] Dafalias YF, Manzari MT. Simple plasticity sand model accounting for fabric change effects. J Eng Mech 2004;130(6):622–34.
- [26] Naesgaard E, Byrne PM, Seid-Karbasi M, Park SS. Modeling flow liquefaction, its mitigation, and comparison with centrifuge tests. In: Proceedings of the geotechnical earthquake engineering satellite conference, osaka, Japan; 2005.
- [27] Seid-Karbasi M, Byrne PM. Seismic liquefaction, lateral spreading, and flow slides: a numerical investigation into void redistribution. Can Geotech J 2007;44(7): 873–90
- [28] Kamai R, Boulanger RW. Single-element simulations of partial-drainage effects under monotonic and cyclic loading. Soil Dynam Earthq Eng 2012;35:29–40.
- [29] Ziotopoulou K, Boulanger RW. Constitutive modeling of duration and overburden effects in liquefaction evaluations. In: Proc., 2nd int. Conf. On performance-based design in earthquake geotechnical engineering. Oakland, CA: Earthquake Engineering Research Institute; 2012.
- [30] Boulanger RW, Ziotopoulou K. Formulation of a sand plasticity plane-strain model for earthquake engineering applications. Soil Dynam Earthq Eng 2013;53:254–67.
- [31] Kamai R, Boulanger RW. Simulations of a centrifuge test with lateral spreading and void redistribution effects. J Geotech Geoenviron Eng 2013;139(8):1250–61.
- [32] Ziotopoulou K, Boulanger RW. Calibration and implementation of a sand plasticity plane-strain model for earthquake engineering applications. Soil Dynam Earthq Eng 2013;53:268–80.
- [33] Boulanger RW, Ziotopoulou K. PM4Sand (Version 3): a sand plasticity model for earthquake engineering applications. Center for Geotechnical Modeling Report No. UCD/CGM-15/01. Davis, Calif: Department of Civil and Environmental Engineering, University of California; 2015.
- [34] Elgamal A, Parra E, Ragheb A, Yang Z. Modeling of cyclic mobility in saturated cohesionless soils. Int J Plast 2003;19(6):883–905.
- [35] Taiebet M, Dafalias YF, Peek R. A destructuration theory and its application to SANICLAY model. Int J Numer Anal Methods GeoMech 2010;34(10):1009–40.
- [36] Andrade JE, Borja RI. Modeling deformation banding in dense and loose fluidsaturated sands. Finite Elem Anal Des 2007;43(5):361–83.
- [37] Byrne PM, Seid-Karbasi M. Seismic liquefaction, lateral spreading, and flow slides: a numerical investigation into void redistribution. Can Geotech J 2007;44(7): 873-90
- [38] Wang Rui, Zhang Jian-Min, Wang Gang. A unified plasticity model for large postliquefaction shear deformation of sand. Comput Geotech 2014;59:54–66.
- [39] Zou You-Xue, Zhang Jian-Min, Wang Rui. Seismic analysis of stone column improved liquefiable ground using a plasticity model for coarse-grained soil. Comput Geotech 2020;125:103690.
- [40] Tasiopoulou P, Gerolymos N. Constitutive modelling of sand: a progressive calibration procedure accounting for intrinsic and stress-induced anisotropy. Geotechnique 2016;66(9):754–70.
- [41] Barrero Andres R, Taiebat Mahdi, Dafalias Yannis F. Modeling cyclic shearing of sands in the semifluidized state. Int J Numer Anal Methods GeoMech 2020;44(3): 371–88.
- [42] Cundall P, Strack ODL. A discrete numerical model for granular assemblies. Geotechnique 1979;29(1):47–65.
- [43] Zeghal M, El Shamy U. A continuum-discrete hydromechanical analysis of granular deposit liquefaction. Int J Numer Anal Methods GeoMech 2004;28(14):1361–83.
- [44] El Shamy U, Zeghal M. Coupled continuum-discrete model for saturated granular soils. J Eng Mech 2005;131(4):413–26.
- [45] El Shamy U, Zeghal M, Dobry R, Thevanayagam S, Elgamal A, Abdoun T, C Medina R Bethapudi, Bennett V. Micromechanical aspects of liquefaction-induced lateral spreading. Int J GeoMech 2010;10(5):190–201.
- [46] Chen F, Drumm EC, Guiochon G. Coupled discrete element and finite volume solution of two classical soil mechanics problems. Comput Geotech 2011;38(5):
- [47] Liu G, Rong G, Peng J, Zhou C. Numerical simulation on undrained triaxial behavior of saturated soil by a fluid coupled-DEM model. Eng Geol 2015;193: 256 66
- [48] Guo Y, Yu XB. Understanding the microscopic moisture migration in pore space using DEM simulation. J. Rock Mech. Geotech. Eng. 2015;7(2):171–7.
- [49] Ravichandran N, Machmer B, Krishnapillai H, Meguro K. Micro-scale modeling of saturated sandy soil behavior subjected to cyclic loading. Soil Dynam Earthq Eng 2010;30(11):1212–25.

- [50] Okada Y, Ochiai H. Coupling pore-water pressure with distinct element method and steady state strengths in numerical triaxial compression tests under undrained conditions. Landslides 2007;4(4):357–69.
- [51] Zhu YI, Fox PJ, Morris JP. A pore-scale numerical model for flow through porous media. Int J Numer Anal Methods GeoMech 1999;23(9):881–904.
- [52] Potapov AV, Hunt ML, Campbell CS. Liquid-solid flows using smoothed particle hydrodynamics and the discrete element method. Powder Technol 2001;116(2–3): 204–13
- [53] Abdelhamid Y, El Shamy U. Pore-scale modeling of surface erosion in a particle bed. Int J Numer Anal Methods GeoMech 2014;38(2):142–66.
- [54] El Shamy U, Abdelhamid Y. Modeling granular soils liquefaction using coupled lattice Boltzmann method and discrete element method. Soil Dynam Earthq Eng 2014;67:119–32.
- [55] Abdelhamid Y, El Shamy U. Pore-scale modeling of fine-particle migration in granular filters. Int J GeoMech 2016;16(3):04015086.
- [56] Jackson R. The dynamics of fluidized particles. Cambridge, U.K.; New York: Cambridge University Press; 2000.
- [57] El Shamy U. A coupled continuum-discrete fluid-particle Model for granular soil liquefaction. PhD Thesis. Troy, NY: Rensselaer Polytechnic Institute; 2004.
- [58] Sun X, Sakai M, Yamada Y. Three-dimensional simulation of a solid-liquid flow by the DEM-SPH method. J Comput Phys 2013;248:147-76.
- [59] Markauskas D, Kruggel-Emden H, Scherer V. Numerical analysis of wet plastic particle separation using a coupled DEM-SPH method. Powder Technol 2018;325: 218–27.
- [60] Markauskas D, Kruggel-Emden H. Coupled DEM-SPH simulations of wet continuous screening. Adv Powder Technol 2019;30(12):2997–3009.
- [61] Yi He, Bayly AE, Hassanpour A, Muller F, Wu K, Yang D. A GPU-based coupled SPH-DEM method for particle-fluid flow with free surfaces. Powder Technol 2018; 338:548–62.
- [62] Robinson M, Ramaioli M, Luding S. Fluid–particle flow simulations using two-way-coupled mesoscale SPH–DEM and validation. Int J Multiphas Flow 2014;59: 121–34.
- [63] Fernandez JW, Cleary PW, Sinnott MD, Morrison RD. Using SPH one-way coupled to dem to model wet industrial banana screens. Miner Eng 2011;24(8):741–53.
- [64] Sinnott MD, Cleary PW, Morrison RD. Combined DEM and SPH simulation of overflow ball mill discharge and trommel flow. Miner Eng. 2017;108:93–108.
- [65] Cleary PW. Prediction of coupled particle and fluid flows using DEM and SPH. Miner Eng 2015;73:85–99.
- [66] Karunasena HCP, Senadeera W, Gu YT, Brown RJ. A coupled SPH-DEM model for micro-scale structural deformations of plant cells during drying. Appl Math Model 2014;38(15–16):3781–801.
- [67] Wu K, Yang D, Wright N. A coupled SPH-DEM model for fluid-structure interaction problems with free-surface flow and structural failure. Comput Struct 2016;177: 141–61.
- [68] Gingold RA, Monaghan JJ. Smoothed particle hydrodynamics: theory and application to non-spherical stars. Mon Not Roy Astron Soc 1977;181(3):375–89.
- [69] Lucy LB. A numerical approach to the testing of the fission hypothesis. Astron J 1977;82:1013–24.
- [70] Monaghan JJ. Smoothed particle hydrodynamics. Annu Rev Astron Astrophys 1992;30(1):543–74.
- [71] Usama El Shamy and Saman Farzi Sizkow. Coupled smoothed particle hydrodynamics-discrete element method simulations of soil liquefaction and its mitigation using gravel drains. Soil Dynam Earthq Eng, 140:106460.
- [72] Anderson TB, Jackson R. Fluid mechanical description of fluidized beds. equations of motion. Ind Eng Chem Fundam 1967;6(4):527–39.
- [73] Dehnen W, Aly H. Improving convergence in smoothed particle hydrodynamics simulations without pairing instability. Mon Not Roy Astron Soc 2012;425(2): 1068–82
- [74] Morris JP, Fox PJ, Zhu Y. Modeling low Reynolds number incompressible flows using SPH. J Comput Phys 1997;136(1):214–26.
- [75] Monaghan JJ. SPH without a tensile instability. J Comput Phys 2000;159(2): 290–311.
- [76] Monaghan JJ. Simulating free surface flows with SPH. J Comput Phys 1994;110(2): 399–406.
- [78] Iwashita K, Oda M. Rolling resistance at contacts in simulation of shear band development by dem. J Eng Mech 1998;124(3):285–92.
- [79] Oda M, Konishi J, Nemat-Nasser S. Experimental micromechanical evaluation of strength of granular materials: effects of particle rolling. Mech Mater 1982;1(4): 269–83.
- [80] Calvetti F, Combe G, Lanier J. Experimental micromechanical analysis of a 2d granular material: relation between structure evolution and loading path. Mechanics of Cohesive-frictional Materials. Int. J. Experiments, Modell. Comput. Mater. Struct. 1997;2(2):121–63.
- [81] Misra A, Jiang H. Measured kinematic fields in the biaxial shear of granular materials. Comput Geotech 1997;20(3–4):267–85.
- [82] Markauskas D, Kruggel-Emden H, Sivanesapillai R, Steeb H. Comparative study on mesh-based and mesh-less coupled CFD-DEM methods to model particle-laden flow. Powder Technol 2017;305:78–88.
- [83] Ergun S. Fluid flow through packed columns. Chem Eng Prog 1952;48:89-94.
- [84] Itasca Consulting Group. PFC3D (particle flow code in 3 dimensions), version 6.0. Minneapolis, MN. 2019.
- [85] Oberkampf W, Trucano T, Hirsch C. Verification, validation, and predictive capability in computational engineering and physics. Technical Report SAND2003-3769. Albuquerque, NM: Sandia National Laboratories; 2003.

- [86] Oberkampf W, Trucano T. Verification and validation in computational fluid dynamics. Technical Report SAND2002-0529. Albuquerque, NM: Sandia National Laboratories; 2002.
- [87] Zamani N, El Shamy U. Analysis of wave propagation in dry granular soils using dem simulations. Acta Geotechnica 2011;6(3):167.
- [88] Saman Farzi Sizkow, El Shamy Usama. SPH-DEM simulations of saturated granular soils liquefaction incorporating particles of irregular shape. Computers and Geotechnics, Acceptde; 2021.
- [89] Iai S, Tobita T, Nakahara T. Generalised scaling relations for dynamic centrifuge tests. Geotechnique 2005;55(5):355–62.
- [90] Carman PC. Fluid flow through granular beds. Trans Inst Chem Eng 1937;15: 150–66.
- [91] Edwards SF. The equations of stress in a granular material. Physica A 1998;249: 226–31.